Materials Today Advances 18 (2023) 100371

Contents lists available at ScienceDirect

Materials Today Advances

journal homepage: www.journals.elsevier.com/materials-today-advances/

Solving the problem of solidification cracking during additive manufacturing of CrMnFeCoNi high-entropy alloys through addition of Cr_3C_2 particles to enhance microstructure and properties

Xintian Wang [a], Zhiyong Ji [a], Robert O. Ritchie [b], Ilya Okulov [c, d], Juergen Eckert [e, f], Chunlei Qiu [a, *]

[a] School of Materials Science and Engineering, Beihang University, Beijing, 100191, China
[b] Department of Materials Science & Engineering, University of California, Berkeley, CA, 94720, USA
[c] Leibniz Institute for Materials Engineering - IWT, Badgasteiner Str. 3, 28359, Bremen, Germany
[d] Faculty of Production Engineering, University of Bremen, Badgasteiner Str. 1, 28359, Bremen, Germany
[e] Department of Materials Science, Chair of Materials Physics, Montanuniversität Leoben, Jahnstraße 12, Leoben, A-8700, Austria
[f] Erich Schmid Institute of Materials Science, Austrian Academy of Sciences, Jahnstraße 12, Leoben, A-8700, Austria

ARTICLE INFO

Article history:
Received 23 February 2023
Received in revised form
4 April 2023
Accepted 14 April 2023
Available online xxx

Keywords:
High-entropy alloys
Selective laser melting
Solidification cracking
Microstructure
Deformation mechanism

ABSTRACT

In this study, TiAl and Cr_3C_2 particles were added to a high-entropy CrMnFeCoNi alloy through powder mixing and selective laser melting (SLM) with the aim of acquiring both high SLM processibility and an excellent combination of high strength and ductility with a post-process aging treatment. By only adding 4 at.% TiAl particles into CrMnFeCoNi, a number of cracks were found in as-printed samples for the processing conditions under investigation, promoted by a considerable increase in solidification range and gradient in the late stage of solidification. However, further addition of 2.5 at.% Cr_3C_2 particles into $(CrMnFeCoNi)_{96}(TiAl)_4$ reduced the solidification range and gradient, allowing to successfully suppress hot cracking. The as-printed $(CrMnFeCoNi)_{96}(TiAl)_4$ samples are characterized by γ grains each containing a group of cells oriented along a similar direction, with the matrix decorated by a small number of nano-sized Al_2O_3 and σ particles and the cell boundaries with segregated Ti. The addition of Cr_3C_2 transformed the segregated Ti at the cell boundaries into discrete TiC nanoparticles. On aging at 650 °C, a high density of long-range ordered domains with considerable B2 and σ precipitates formed. Compared to the SLM-processed CrMnFeCoNi, the as-printed $(CrMnFeCoNi)_{96}(TiAl)_4$ displays a reduced 0.2% yield strength and significantly reduced ductility due to the presence of cracks. Conversely, the as-printed $(CrMnFeCoNi)_{96}(TiAl)_4 + Cr_3C_2$ samples showed a slightly enhanced yield strength and considerably improved UTS. Aging significantly improves both strength properties while maintaining the good ductility. The long-range ordered domains and precipitation clearly are effective in impeding dislocation motion and can be considered to be the prime source of the increased strength of the dual-particle containing alloy.

1. Introduction

High-entropy alloys (HEAs) are considered to be promising for applications in space, aerospace and nuclear industries owing to their high strength, good ductility, high cryogenic toughness and excellent corrosion resistance [1–5]. Face-centered cubic (FCC) HEAs, such as CrMnFeCoNi, and body-centered cubic (BCC) HEAs, such as AlCrFeCoNi are some of the most common HEAs. The former alloys are characterized by high ultimate tensile strength (UTS) and ductility but rather low yield strength (YS < 300 MPa in the conventionally cast condition) while the latter shows high compressive strength and ductility but poor tensile properties. To achieve both high strength and good ductility in HEAs, one potent method is to develop precipitate-strengthened HEAs based on an FCC γ matrix. The most common approach is to add Ti and/or Al into FCC HEAs to promote precipitation and strengthening [6–10].

In this regard, the use of non-traditional manufacturing processes such as additive manufacturing (AM) can be used to help

* Corresponding author.
E-mail address: chunlei_qiu@buaa.edu.cn (C. Qiu).

https://doi.org/10.1016/j.mtadv.2023.100371

improve the mechanical properties of HEAs by their unique processing characteristics. For example, due to its rapid solidification and cooling characteristics, selective laser melting (SLM) allows for the formation of fine grains and numerous nano-sized cell structures with a high density of dislocations in HEAs such as CrMnFeCoNi, which leads to immediate improvements in the yield strength, by as much as 250 MPa, as compared with the properties of conventionally manufactured counterparts [11–13].

However, the majority of HEAs have been found to be susceptible to hot tearing during additive manufacturing (AM). For example, HEAs such as $Al_xCrFeCoNi$ (x = 0–1.0), $Al_xCrCuFeNi_2$ (x = 0–1.0), $AlCrCuFeNi_x$ (x = 0–2.5) and $(CrMnFeCoNi)_{96}(TiAl)_4$ have all been reported to develop hot tearing cracks during SLM [14–18]. Hot tearing, also known as hot cracking or solidification cracking, happens at the final stage of the solidification process where the material exists in a partly solid state [19]. When there is a lack of compensation by liquid flow, the partly solid material can be torn apart under the thermal stresses induced by solidification shrinkage [20]. The solidification cracks usually have smooth surfaces indicating the presence of a liquid film during crack formation [21]. Further, above the solidus temperature, cavities and pores are prone to form in the semi-solid zone and can provide initiation sites for insipient cracks [22]. The semi-solid zone, which is determined by the solidification range or freezing range (*i.e.*, the range between the liquidus and solidus temperatures), is critical for the susceptibility to solidification cracking. A limited solidification range generates a narrow semi-solid mush and thus helps reduce the susceptibility to cracking. A number of studies have shown that the cracking susceptibility of an alloy during additive manufacture is highly associated with the solidification range [23–26], indicating that this feature represents a highly effective index for evaluating the cracking susceptibility. Kou [27], for example, acknowledged the importance of the very last stages of solidification and demonstrated that a steeper gradient between the temperature and the fraction of solid (*i.e.*, solidification gradient) resulted in a higher susceptibility to solidification cracking of the material. Therefore, we can conclude that a material with a lower solidification gradient should have an improved resistance to solidification cracking. The solidification gradient, which is defined as $dT/d(f_s^{1/2})$, where f_s is the solid fraction and T is the temperature, is thus another critical index for evaluating the susceptibility to solidification cracking. Indeed, this index has been verified by experimental data for the casting and welding of several aluminum alloys [27]. Despite significant similarities between fusion welding and fusion additive manufacturing, such as SLM, these concepts have not been widely used to assess the cracking susceptibility in fusion AM processing. Recently, Tang et al. [24] successfully used the solidification index to rationalize the solidification cracking susceptibility of several advanced nickel-based superalloys during SLM. However, more work is needed to validate this theory for the fusion AM of a broader set of materials systems given that the cooling rate during SLM is usually higher, *i.e.*, reaching 10^6–10^7 K/s, than that in arc and laser/electron beam welding [28,29]. We believe that it is particularly relevant for the additive manufacturing of HEAs to use these solidification cracking indices to evaluate the effects of the solidification characteristics on their susceptibility to cracking.

Recently, local compositional variations during solidification have been recognized to be important for the development of cracking and the overall mechanical performance in a number of alloys [15,25]. Sun et al. [25], for example, found that a high Si content in Inconel 738LC promoted the segregation of B at interdendritic regions during solidification which led to a reduction in the solidus temperature in these regions, thereby increasing the cracking susceptibility. Reducing the amount of Si to a low level (0.03 wt%) was found to fully suppress hot cracking during SLM. Al was also found to segregate into the interdendritic regions of the $Al_{0.5}CrFeCoNi$ HEA during solidification to form ordered B2 NiAl and disordered BCC Cr phases which, by accommodating residual strains, served to reduce the cracking susceptibility during AM [15]. These studies indicate that there is a good potential to suppress solidification cracking through segregation via grain-boundary engineering.

In this study, our objective was to improve the processibility of the high-entropy alloy $(CrMnFeCoNi)_{96}(TiAl)_4$ upon SLM by adding a small amount of Cr_3C_2 to promote segregation of C at interdendritic regions and grain boundaries. The rationale behind this is that recent studies have indicated that an increasing C content is beneficial to the AM processibility of some alloys such as Inconel 738 and AlCrFeCoNi. For example, Zhou et al. [26] reported that increasing the carbon content in Inconel 738 promoted the formation of more granular monocarbides along the boundaries of the cellular structure while significantly reducing the low melting-point phases containing boron and γ/γ' eutectics at these boundaries, a phenomenon which markedly decreased any susceptibility for cracking during SLM. Further, Pan et al. [30] found that C segregation at inter-dendritic regions of AlCrFeCoNi during SLM promoted the formation of an FCC network structure which significantly reduced solidification cracking. The selection of Cr_3C_2 for the present study is because this carbide shows a relatively low melting point (1890 °C) as compared with many other carbides such as TiC and NbC so that they can be more easily melted during SLM, favouring the introduction of C into the alloy. As these studies have not been substantiated by thermodynamic and kinetic rules related to solidification behavior, here we specifically investigate the influence of the addition of Cr_3C_2 on the solidification behavior, microstructure and cracking susceptibility of $(CrMnFeCoNi)_{96}(TiAl)_4$, through both thermodynamic simulation and experimental approaches. Additionally, by eliminating such solidification cracking through Cr_3C_2 additions and by appropriate post-process aging, our intent was to maximize the strength of the alloy without compromising ductility in the alloy. The underlying concept is to produce crack-free samples in the as-printed state prior to applying as low aging temperatures as possible to promote the formation of long-range ordered (LRO) $L1_2$ domains as well as Heusler and B2 precipitates while retaining a nano-sized cell structure and a high density of dislocations that are essential for the strength of the material. In our previous studies [18,31], hot isostatic pressing (HIPing) was performed on the SLM-processed $(CrMnFeCoNi)_{96}(TiAl)_4$, which fully eliminated cracks but also removed the nano-sized cell structures and dislocations; although numerous LRO $L1_2$ domains and Heusler, B2 and σ particles were formed in the matrix, the post-HIP aging did not lead to any pronounced improvements in yield strength [31]. The current work demonstrates how both cell structures and LRO $L1_2$ domains, together with various precipitation sequences, are essential for the strength improvement of FCC HEAs.

2. Materials and methods

Argon atomized equiatomic CrMnFeCoNi high-entropy alloy powder and Ti–48Al–2Cr–2Nb (TiAl) powder both with a particle size range of 15–53 μm were first blended for 6 h at a rotation speed of 28 rpm in an argon atmosphere using a three-dimensional (3D) swing powder mixer. The two types of powder were mixed with an atomic ratio of 96:4 to prepare $(CrMnFeCoNi)_{96}(TiAl)_4$ alloy samples. The powder particles were then further mixed in argon with 2.5 at.% Cr_3C_2 powder particles (with an average diameter of 2.5 μm) which is equivalent to the addition of 1 at.% C, by using a

horizontal cylindrical ball mill. To be mentioned, we only add 1 at.% C because according to previous study [30], addition of 2 at.% C to AlCrFeCoNi already caused pronounced segregation of C along cell boundaries and formation of FCC network; in this study, we aim to avoiding cracking by adding a small amount of C without changing the microstructure significantly. A ball-to-powder weight ratio of 4:1 with balls of 5 mm diameter were used for the powder mixing. The milling process took 10 min with a shaft rotation speed of 600 rpm. Cr_3C_2 was added as ultrafine particles as they have the highest melting point among the mixed powder particles. Fine particles were expected to be favorable for complete melting during SLM. Both the $(CrMnFeCoNi)_{96}(TiAl)_4$ and $(CrMnFeCoNi)_{96}(TiAl)_4 + Cr_3C_2$ (hereafter referred to as HTC) powder mixtures were then processed using a Renishaw AM 400 system equipped with a ytterbium fiber laser. Samples with a dimension of 60 × 10 × 11 mm^3 were fabricated in an argon atmosphere for microstructural characterization and tensile testing. The AM processing conditions for sample preparation are summarized in Table 1. A Meander scanning strategy was used for hatch scanning on each layer and the scanning direction was rotated by 67° for each layer. The volumetric energy density (VED), which is defined below, was used to evaluate the input energy density:

$$VED = \frac{P*t}{d_h*d_p*l}\left[\mathrm{J/mm^3}\right], \quad (1)$$

where P is the laser power, t is the exposure time, d_h is the hatch distance, d_p is the point distance and l is the powder layer thickness.

Some of the as-fabricated samples were subjected to an aging treatment at 650 °C for 30 h in a vacuum furnace (10^{-4} Pa) followed by air cooling. The aging temperature was selected to promote precipitation and improve the tensile strength while maintaining the unique microstructural features of the as-printed state; these include the cell structures and dislocations that are beneficial for the tensile properties. In our previous study [31], we demonstrated that aging at 650 °C can promote the formation of LRO $L1_2$ domains as well as Heusler and B2 in SLM + HIPed $(CrMnFeCoNi)_{96}(TiAl)_4$ while minimizing formation of brittle σ phase.

The as-printed and SLM-processed plus aged samples were longitudinally sectioned by electrical discharge machining (EDM) and ground using SiC papers from 320 grit up to 2400 grit before being polished using 3 μm diamond suspension and colloidal silica suspension (or OPS solution). The samples were then electrolytically etched in a solution which contained 10 g oxalic acid and 100 ml water for microstructural characterization using a LEICA DM4000 optical microscope (OM) and a SUPRA55 scanning electron microscope (SEM). A JEOL JSM-7900 F SEM microscope which was fitted with an electron backscatter diffraction (EBSD) detector was used for grain structure and texture analysis. Transmission electron microscopy (TEM) examination was also performed on the samples using a FEI TecnaiG20 FEG TEM microscope fitted with an Oxford EDS detector. Disc specimens with a diameter of 3 mm and a thickness of 40–50 μm were prepared and then electropolished using a twin-jet electro-polishing equipment in a solution of 5 vol% perchloric acid and 95 vol% alcohol. The TEM experiments were conducted at an accelerating voltage of 200 kV.

Uniaxial tensile tests were performed on the as-printed and SLM-processed and aged samples. Tensile test pieces with a gauge length of 23 mm and a reduced section diameter of 4 mm were machined out of the horizontally built samples. The tensile testing was carried out at a nominal strain rate of 5×10^{-4}/s. After the tensile testing, the fracture surfaces and longitudinal sections of the tested specimens were examined using SEM and their deformation structures were investigated by TEM.

3. Results

3.1. SLM processibility and chemical homogeneity

Fig. 1 shows the morphology and distribution of the mixed CrMnFeCoNi, TiAl and Cr_2C_3 powder particles. It is clear that the different sized powder particles have mixed well (Fig. 1a). EDS mapping results show that the TiAl powder particles are uniformly distributed among the CrMnFeCoNi powder particles (Fig. 1b and c) while the Cr_2C_3 powder particles are homogeneously assembled onto the surfaces of large alloy particles. The majority of the alloy powder particles remain spherical after mixing. These results indicate that the present powder mixing strategy was effective in homogeneously distributing different types of powder particles with different sizes.

Fig. 2 shows the defect distribution in the SLM-processed $(CrMnFeCoNi)_{96}(TiAl)_4$ samples with and without the addition of Cr_2C_3. It is clear that the as-printed $(CrMnFeCoNi)_{96}(TiAl)_4$ samples all contain a considerable number of cracks, which tend to increase with increased energy density. In contrast, the samples with the addition of Cr_2C_3 are all crack-free (see Fig. 2d–f and Supplementary Fig. 1). These results indicate that the addition of Cr_2C_3 enhances the SLM processibility of the $(CrMnFeCoNi)_{96}(TiAl)_4$ alloy significantly. Detailed SEM examination of the cracks formed in the as-printed $(CrMnFeCoNi)_{96}(TiAl)_4$ samples revealed that cracking tends to occur at the triple junctions of several adjacent grains where dendritic structures are present (Fig. 3a); this is often typical of solidification cracking. A number of vertically elongated cracks with sharp kinks are also evident; based on our SEM studies, these were also associated with dendritic structures (Fig. 3b and c) and usually are an indication of solid-state cracking or strain-age cracking [24]. EBSD analysis revealed that several cracks formed predominantly along high-angle grain boundaries (HAGBs), as shown in Fig. 4a. Kernel average misorientation (KAM) distribution maps (Fig. 4c) indicated that the cracking sites displayed much higher KAM values than the other regions. Given that the density of geometrically necessary dislocations (GNDs) is proportional to local misorientation angles, the higher KAM values imply that the crack

Table 1
Laser powder bed fusion processing parameters used in the current study.

Processing condition	Laser power, W	Exposure time, μs	Point distance, μm	Hatch distance, μm	Layer thickness, μm	Energy density, J/mm^3
1	250	60	60	90	50	55.6
2		90				83.3
3		120				111.1
4	325	60	60	90	50	72.2
5		90				108.3
6		120				144.4
7	400	60	60	90	50	88.9
8		90				133.3
9		120				177.8

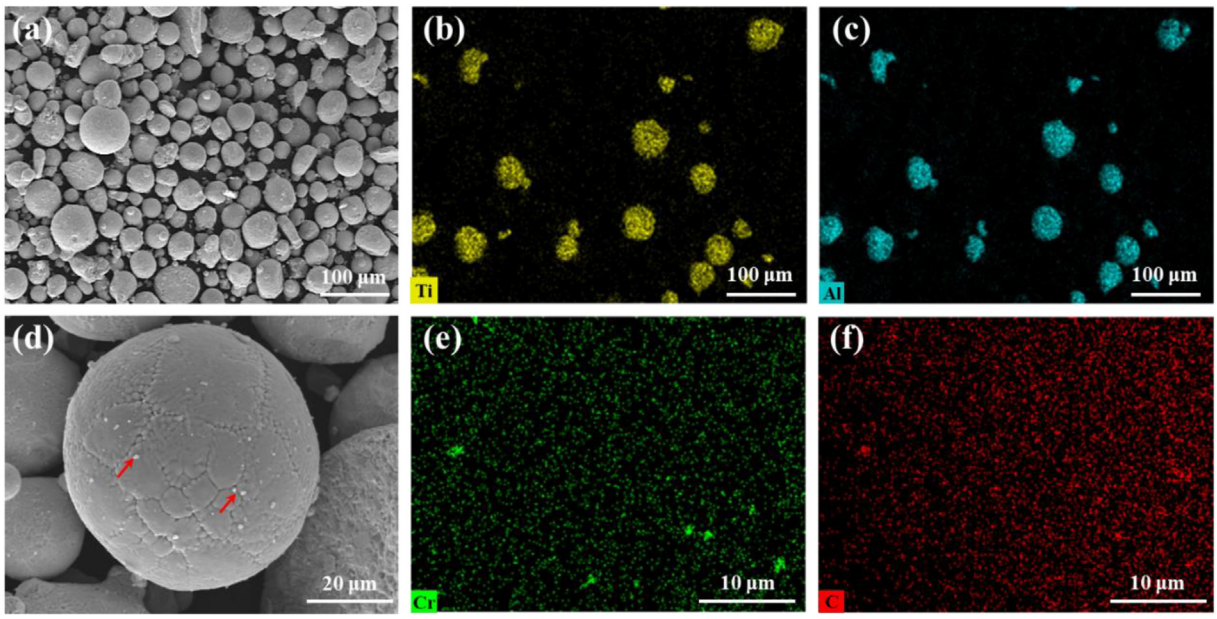

Fig. 1. (a,d) SEM micrographs showing the distribution and morphology of the mixed CrMnFeCoNi, TiAl, and Cr_3C_2 powder particles; EDS mapping results showing (b,c) the distribution of TiAl powder particles among the mixed powder particles and (e,f) the distribution of Cr_3C_2 particles on an alloy powder particle. The arrows in (d) refer to the presence of small Cr_3C_2 particles on a large alloy powder particle.

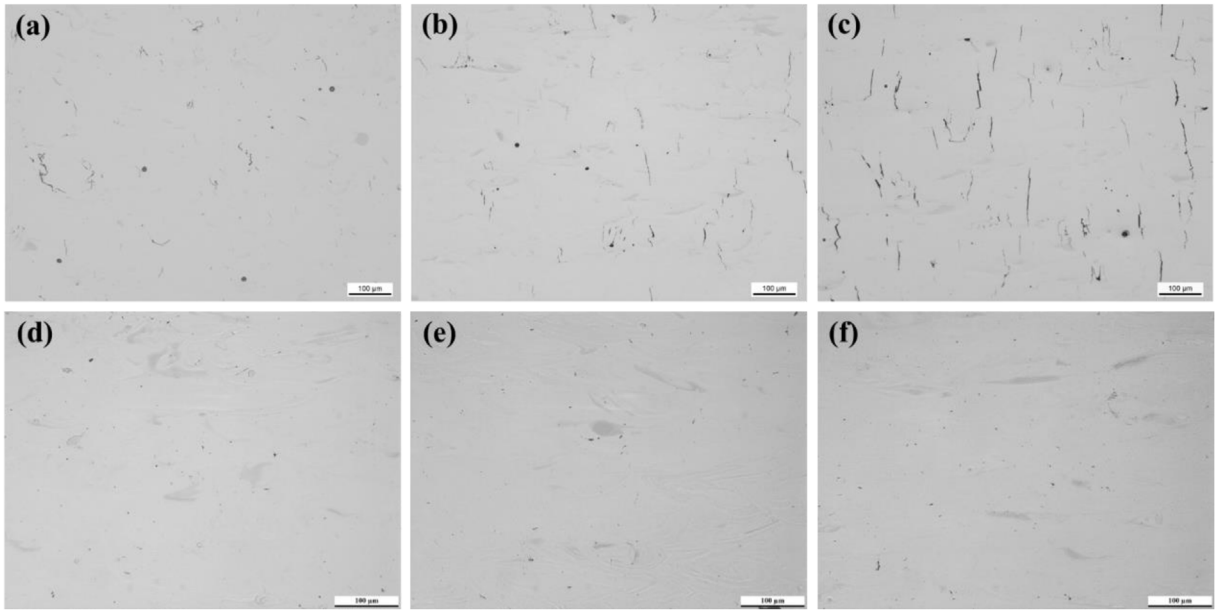

Fig. 2. Optical micrographs showing the distribution of defects in the as-printed (a–c) $(CrMnFeCoNi)_{96}(TiAl)_4$ and (d–f) $(CrMnFeCoNi)_{96}(TiAl)_4$ + 2.5 at.% Cr_3C_2 alloy samples. The samples shown in the left column were fabricated with 250 W-60 μs, those in the middle column were made with 325 W-60 μs, and those in the right column were produced at 400 W-60 μs?

initiation sites contain higher GND densities and thus would have experienced higher strains than the surrounding regions.

Fig. 5 shows the microstructure of the as-printed $(CrMnFeCoNi)_{96}(TiAl)_4 + Cr_2C_3$ samples fabricated under different AM processing conditions. A number of incompletely melted TiAl particles can be seen in the samples made with low energy densities, *i.e.*, at 250 W-60 μs, 250 W-90 μs and 400 W-60 μs. These particles are grey and are usually elliptical or irregular-shaped; they can be identified as TiAl particles from the point EDS analysis provided in Fig. 6a–d and Table 2. The number density of the unmelted TiAl particles generally decreases with increasing laser power and exposure duration (Fig. 7a). With higher processing energy densities such as 250 W-120 μs, 400 W-90 μs and 400 W-120 μs, almost no unmelted particles are observed, although there are considerable arc-shaped grey or black belt structures/regions present in all samples. These belt structures are all located at the bottom of the solidified melt pools and from the EDS mapping analysis revealed that they are enriched in Ti and Al (Fig. 6f and g), indicating that they formed due to segregation of these elements at the bottom of these melt pools. Similar chemically-segregated

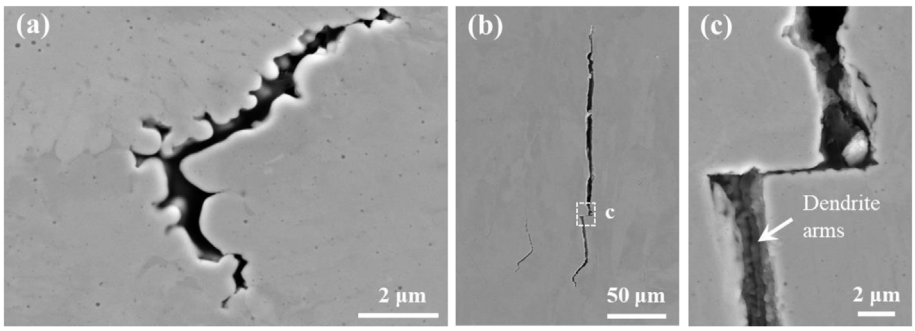

Fig. 3. SEM micrographs showing (a) a crack at a triple junction of several adjacent grains and (b) a vertically elongated crack in an as-printed $(CrMnFeCoNi)_{96}(TiAl)_4$ sample; (c) an enlarged view of the kink shown in (b).

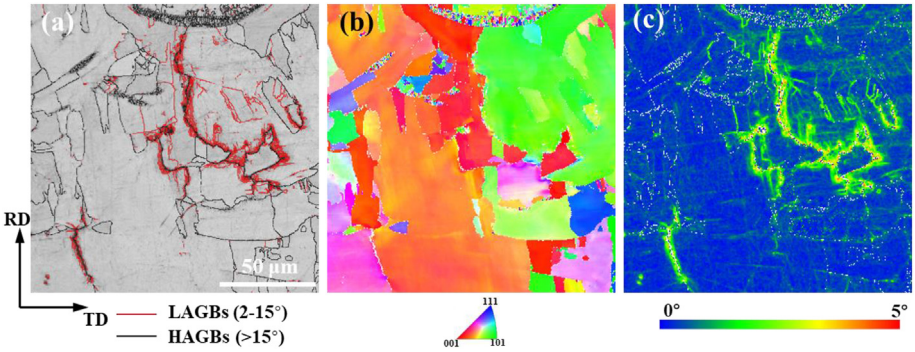

Fig. 4. (a) EBSD image quality map and (b) inverse pole figure (IPF) color map showing cracks and grain structure in the $(CrMnFeCoNi)_{96}(TiAl)_4$ sample fabricated at 250 W-60 μs, (c) Kernel average misorientation (KAM) map of the sample. (For interpretation of the references to color in this figure legend, the reader is referred to the Web version of this article.)

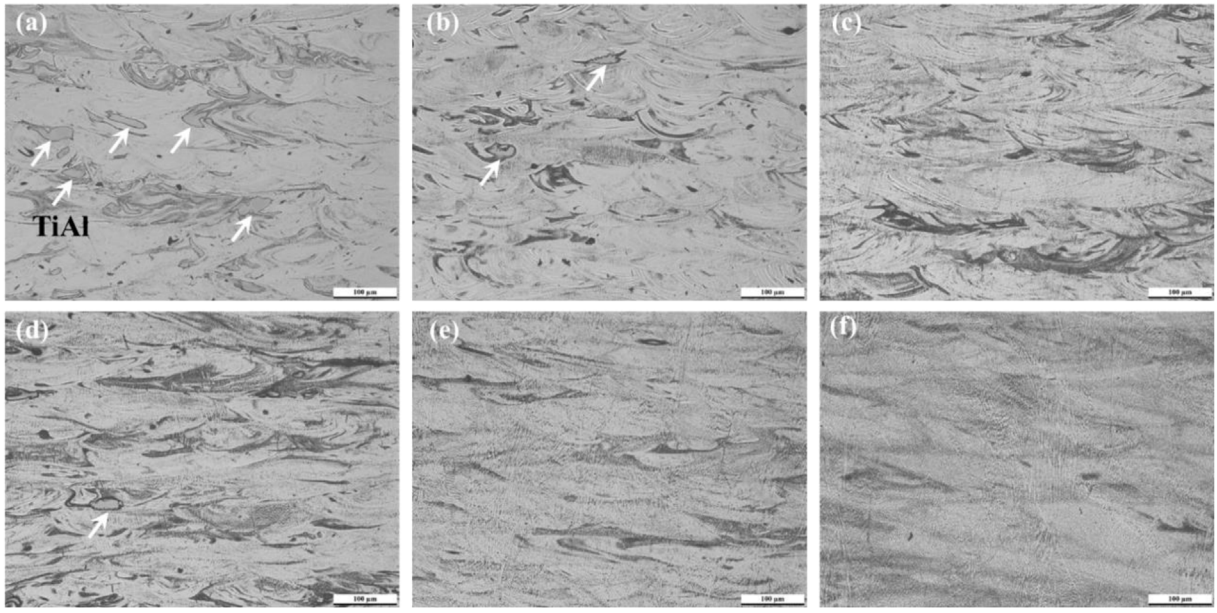

Fig. 5. Optical micrographs showing the microstructure in the as-printed $(CrMnFeCoNi)_{96}(TiAl)_4 + Cr_3C_2$ alloy samples built under different processing conditions, with energy densities of (a) 250 W-60 μs, (b) 250 W-90 μs, (c) 250 W-120 μs, (d) 400 W-60 μs, (e) 400 W-90 μs, and (f) 400 W-120 μs?

regions have been reported in a number of previous studies [32,33], and have been generally attributed to an inhomogeneous thermal distribution and melt flow behavior within the melt pools. It is noted that at 250 W, the area fraction of the Ti- and Al-segregated belt regions appears to increase with an increasing duration of laser exposure, whereas at 400 W, these regions decrease continuously with increased exposure duration (Figs. 5 and 7b). This is deemed to be associated with the higher laser exposure duration at 250 W aiding the melting of more TiAl particles, which favored the creation of more Ti- and Al-segregated belt regions. At 400 W, since the

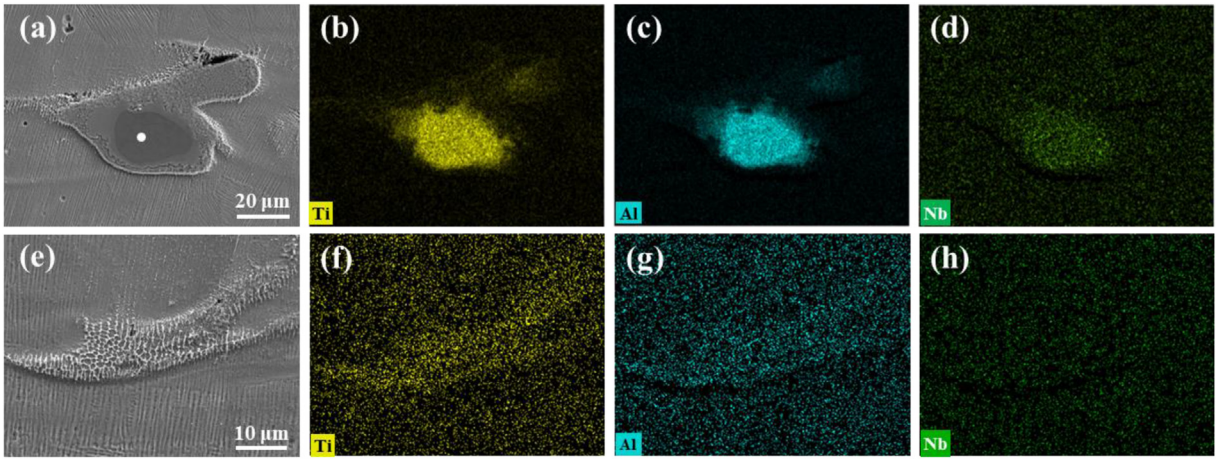

Fig. 6. (a) SEM micrograph showing an unmelted powder particle in an as-printed $(CrMnFeCoNi)_{96}(TiAl)_4 + Cr_3C_2$ sample; (b–d) EDS mapping analysis results showing the elemental distribution in the unmelted particle; (e) SEM micrograph showing an arc-shaped belt region at the bottom of a solidified melt pool; (f–h) EDS mapping analysis results showing the chemical distribution at and around the belt region.

Table 2
Nominal composition (at.%) of the as-received TiAl alloy powder and the point SEM-EDS analysis results on an unmelted TiAl powder particle shown in Fig. 6a in an as-printed $(CrMnFeCoNi)_{96}(TiAl)_4$ sample.

Elements	Ti	Al	Nb	Cr
Nominal composition	48	48	2	2
EDS results	52.2	44.1	1.9	1.8

majority of TiAl particles can be melted even within a short exposure duration of 60 μs, increased laser exposure or energy density can promote chemical homogenization within each melt pool and serve to progressively diminish the chemically-segregated regions. A quantitative analysis of the dependence of the area fraction of the Ti- and Al-segregated regions on laser energy density (Fig. 7c) also indicates that the intermediate energy densities are most favorable for the formation of this type of chemically-segregated belt regions. Low and high energy densities did not cause the most belt regions but the mechanisms were clearly different.

3.2. Microstructure

Fig. 8 shows the grain structure in the as-printed $(CrMnFeCoNi)_{96}(TiAl)_4 + Cr_2C_3$ samples fabricated under different processing conditions. The samples built with a relatively low energy density such as 400 W-60 μs contains both large (>50 μm) and fine (<10 μm) grains, the majority having an aspect ratio below 3. With higher energy densities, the grains become increasingly elongated and coarser. Given that there is a high density of chemically segregated regions in the sample made at 400 W-60 μs, the epitaxial grain growth may have been interrupted by the presence of these regions, which can lead to the formation of relatively shorter columnar grains. With increased energy density, these types of segregated regions can be progressively suppressed, leading to more pronounced epitaxial grain growth. Quantitative analysis of the EBSD data in Fig. 8c shows that the samples made at 400 W-60 μs contained the highest fraction of fine grains (<20 μm) with a lower fraction of coarse grains (>20 μm in equivalent diameter) as compared with the samples manufactured with higher energy densities such as 250 W-120 μs and 400 W-120 μs. Interestingly, statistics on the grain-boundary misorientations (Fig. 8d) indicate that the samples made with the higher energy

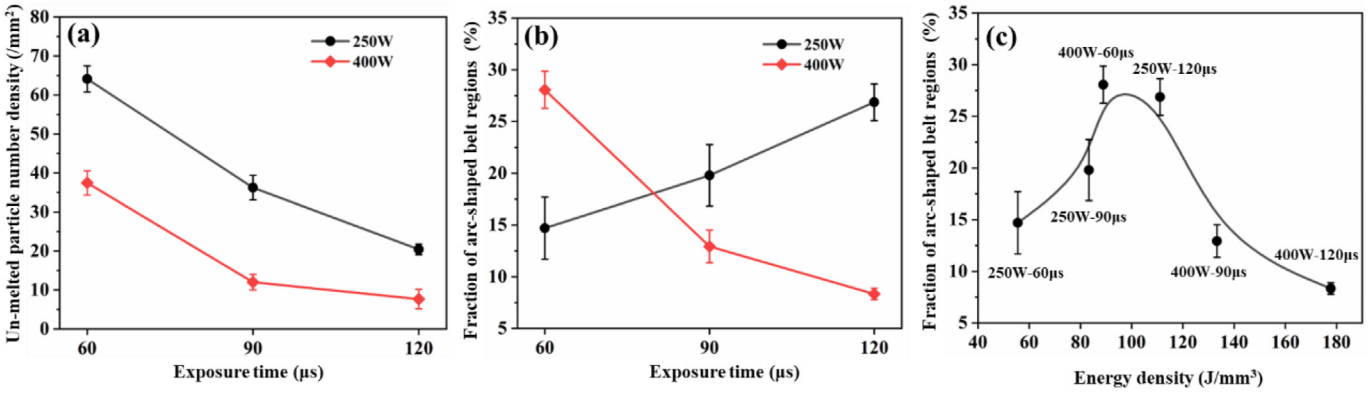

Fig. 7. Graphs showing the dependence of (a) the number density of unmelted TiAl particles, (b) the area fraction of arc-shaped Ti- and Al-segregated regions on laser power and exposure duration in the as-printed $(CrMnFeCoNi)_{96}(TiAl)_4 + Cr_3C_2$ alloy samples and (c) the area fraction of arc-shaped Ti- and Al-segregated regions on laser energy density.

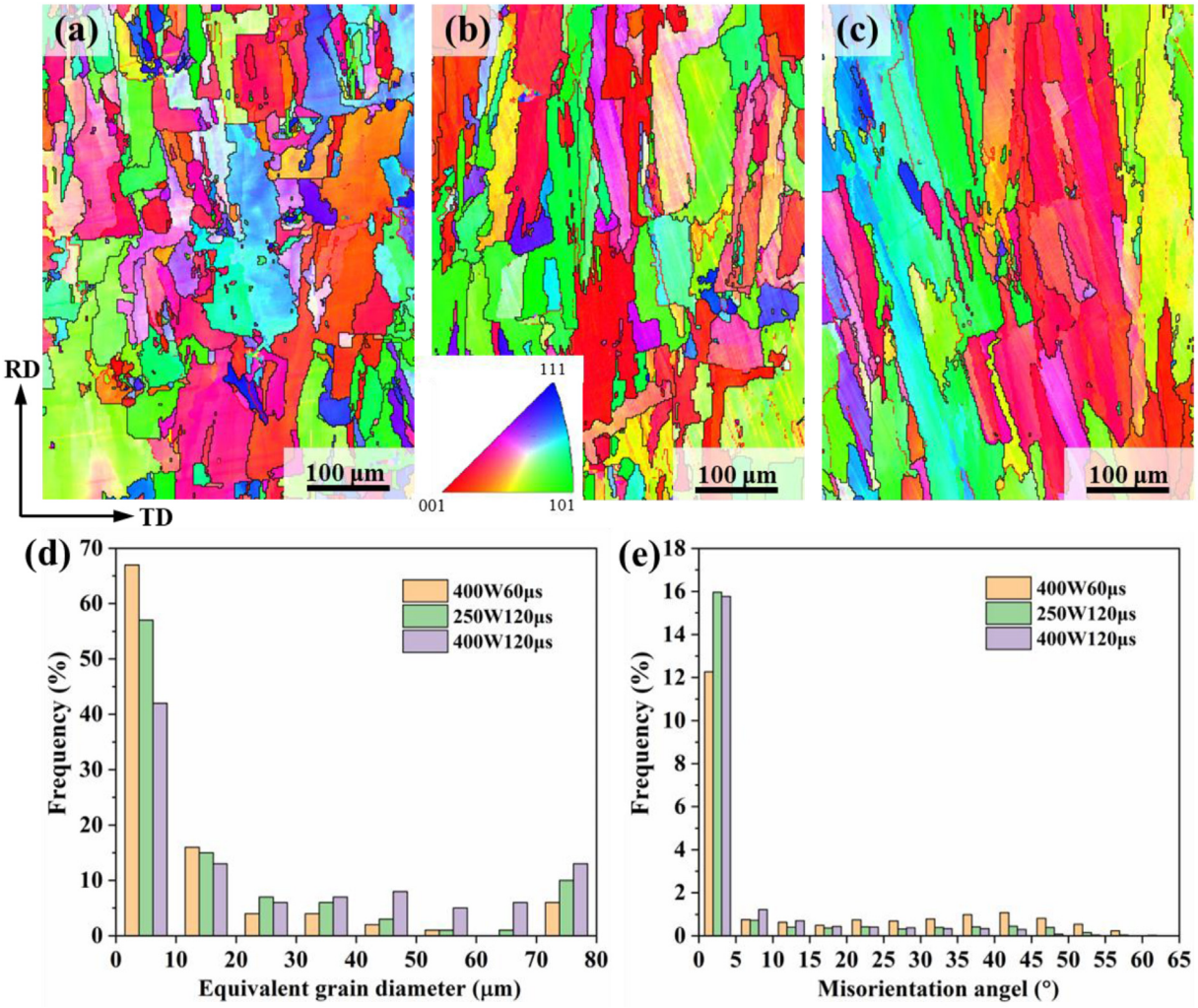

Fig. 8. EBSD IPF color maps showing the grain structures in the samples made at (a) 400 W-60 μs, (b) 250 W-120 μs, (c) 400 W-120 μs and graphs showing the grain size and grain-boundary misorientation distribution in the $(CrMnFeCoNi)_{96}(TiAl)_4 + Cr_3C_2$ samples synthesized with different processing conditions. (For interpretation of the references to color in this figure legend, the reader is referred to the Web version of this article.)

densities display a remarkably higher fraction of low-angle grain boundaries (LAGBs, <15°), suggesting that there should be more grains having similar crystallographic orientations in these microstructures. Pole figures of the three investigated samples (Fig. 9) show that all of them contain more or less <001> texture; further, the texture intensity increases with increased energy density, which is consistent with the grain-boundary misorientation results.

Fig. 10 shows the microstructure in the as-printed $(CrMnFeCoNi)_{96}(TiAl)_4$ samples. The as-fabricated samples are composed of numerous cell structures with higher dislocation densities in the cell boundaries (Fig. 10a), leading to a complex dislocation network. From the TEM-EDS mapping analysis in Fig. 11a, these cell boundaries were found to be covered with segregated Ti, with the matrix decorated by a number of nano-sized, homogeneously distributed, Al_2O_3 particles (Fig. 10b and c). There is also a limited number of relatively larger precipitates that were identified to be σ phase from TEM diffraction pattern analysis (Fig. 10c and d). These precipitates exhibited a specific crystallographic orientation relationship with the matrix, namely $[\bar{1}\ 10]_\sigma//[312]_\gamma$, $(11\ \bar{2})_\sigma//(\bar{1}11)_\gamma$.

Cell structures were also found in the as-printed $(CrMnFeCoNi)_{96}(TiAl)_4 + Cr_2C_3$ samples (Fig. 12) with the cell diameter/width tending to increase with increasing energy density. Aging treatments did not cause obvious changes in these cell structures. The cell boundaries in the as-printed $(CrMnFeCoNi)_{96}(TiAl)_4 + Cr_2C_3$ samples are decorated by a number of precipitates (Figs. 11b and 13b), which from EDS mapping were also found to be enriched in Ti (Fig. 11b). TEM diffraction analysis on the precipitates along the cell boundaries confirmed that the precipitates were TiC particles (Fig. 13c). In addition to TiC particles at cell boundaries and grain boundaries, there are a number of nano-sized Al_2O_3 particles homogeneously distributed in the matrix. From high-resolution TEM (HRTEM) analysis and Fast Fourier Transform (FFT) patterns, the matrix was identified to be pure γ phase, with the cell boundaries displaying a high density of dislocations. Surprisingly, after aging at 650 °C, both the cell structures and the high density of dislocations were retained (Fig. 13f) (which is beneficial to tensile properties), although the aging did result in the formation of a much higher population of σ precipitates that tended to form along grain boundaries in large sizes, *i.e.*, 400–500 nm in length and 150–200 nm in width (Fig. 13g). Precipitation of the B2 phase, with a length and width of ~150 nm and 50 nm, was also observed in the matrix (Fig. 13h). The HRTEM image in Fig. 13i shows no sign of any precipitate in the γ matrix but there are clear $L1_2$ superlattice reflections in the FFT pattern (the inset), suggesting that LRO $L1_2$ domains should have

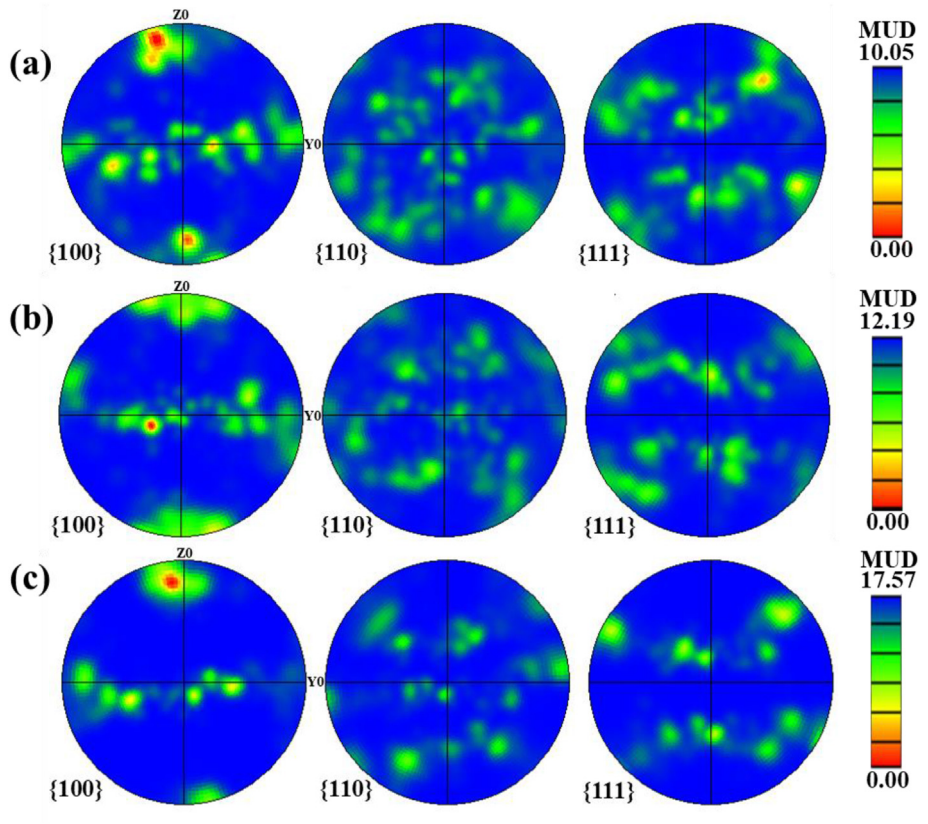

Fig. 9. EBSD pole figures of the as-printed $(CrMnFeCoNi)_{96}(TiAl)_4 + Cr_3C_2$ samples processed at (a) 400 W-60 μs, (b) 250 W-120 μs, (c) 400 W-120 μs, respectively.

formed. This is further verified by the inverse FFT figure shown in Fig. 13j where LRO $L1_2$ domains with sizes between 2 nm and 10 nm in diameter are clearly present and homogeneously distributed in the matrix.

3.3. Tensile behavior

Fig. 14a and Table 3 show the tensile properties of the as-printed and SLM-processed plus aged $(CrMnFeCoNi)_{96}(TiAl)_4 + Cr_3C_2$ samples, which are compared with the corresponding properties of the $(CrMnFeCoNi)_{96}(TiAl)_4$ samples (manufactured at 250 W-60 μs to display the lowest crack and pore densities) and the as-printed CrMnFeCoNi alloy. The as-printed CrMnFeCoNi alloy displays a high yield strength of ~600 MPa with a ductility (% elongation) of 27%. Additions of only TiAl with SLM processing led to a marked degradation in tensile properties with the yield strength reduced to <550 MPa and the ductility to as low as ~7%, which can be attributed to the introduction of cracks, as described above (Fig. 2a). However, further additions of Cr_3C_2, which successfully suppressed cracking during SLM, led to a remarkable improvement in the yield and ultimate tensile strengths together with an enhanced ductility. In particular, the $(CrMnFeCoNi)_{96}(TiAl)_4 + Cr_3C_2$ samples processed with high energy densities (250 W-120 μs, 400 W-90 μs and 400 W-120 μs) which minimize the extent of unmelted TiAl particles, all show high ductilities exceeding 17%. In contrast, the $(CrMnFeCoNi)_{96}(TiAl)_4 + Cr_3C_2$ sample made at 400 W-60 μs, which still contains considerable unmelted TiAl particles, exhibited a reduced ductility of ~10%. Aging significantly elevates the yield (~750 MPa) and ultimate tensile (~950 MPa) strengths of the SLM-processed $(CrMnFeCoNi)_{96}(TiAl)_4 + Cr_3C_2$ samples while maintaining a reasonable ductility (~10%).

Simultaneous additions of TiAl and Cr_3C_2 to CrMnFeCoNi with SLM processing also led to significant enhancement in strain-hardening rates at true strains between ~2% and 15% (Fig. 14b). Aging at 650 °C further enhanced the strain-hardening rates at true strains between ~2% and 9%, but resulted in an earlier failure compared to the unaged samples. Simply adding TiAl to CrMnFeCoNi did not lead to any obvious improvement in strain hardening but caused a much earlier failure, which is suspected to be associated with the presence of cracks in the as-printed material.

Fig. 15 displays the tensile fracture surfaces of the different samples investigated in this study. A number of dendritic structures can be seen on the fracture surface of the as-printed $(CrMnFeCoNi)_{96}(TiAl)_4$ samples. Given that dendritic structures are indicative of the presence of solidification cracks, their presence strongly suggests that pre-existing solidification cracks were responsible for the premature fracture of this material. The as-printed $(CrMnFeCoNi)_{96}(TiAl)_4 + Cr_3C_2$ samples manufactured at high energy densities all show a rough and highly dimpled fracture surface (Fig. 15d–i), indicating that they are highly ductile, which is consistent with the tensile testing results. The SLM-processed and aged $(CrMnFeCoNi)_{96}(TiAl)_4 + Cr_3C_2$ sample, however, failed in an intergranular mode, as evidenced by the fracture surface presented in Fig. 15j-l. SEM imaging of the longitudinal sections of the fracture tensile specimens (Fig. 16) indicates that cracks preferentially initiated from the unmelted TiAl particles and at the bottom regions of the solidified melt pools which correspond to the arc-shaped Ti- and Al-segregated regions. In the SLM-processed and aged samples, in addition to the cracks initiated at the site of unmelted TiAl particles (Fig. 16e), there is further evidence of intergranular cracks (Fig. 16d and f) which are believed to be associated with the presence of the grain-boundary σ phase.

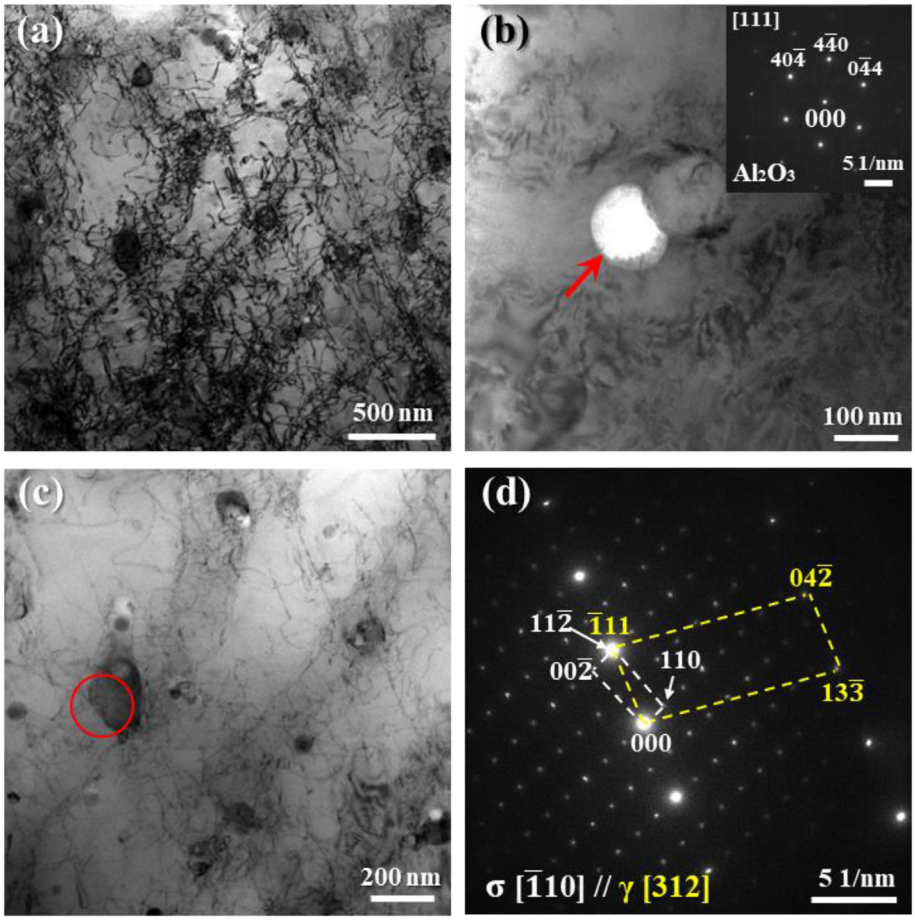

Fig. 10. TEM micrographs showing (a) cell structures and (b–c) precipitates in an as-printed $(CrMnFeCoNi)_{96}(TiAl)_4$ sample; (d) crystallographic orientation relationship between the precipitate shown in (c) and its surrounding matrix.

TEM studies were also performed on the SLM-processed and aged $(CrMnFeCoNi)_{96}(TiAl)_4 + Cr_3C_2$ samples to investigate the source of their higher strength. The images shown in Fig. 17 indicate that deformation occurred by slip of the high density of dislocations in the matrix, whereas Orowan bypassing is evident in the presence of the TiC, Al_2O_3 and σ precipitates (Fig. 17a–c). In addition, HRTEM studies also revealed the presence of stacking faults (Fig. 17d), which were confirmed by corresponding FFT patterns, and in certain localized regions deformation twins (Fig. 17e and f). It seems that multiple deformation mechanisms had been activated during the tensile deformation of the alloy.

4. Discussion

4.1. SLM processibility

It is well known that the CrMnFeCoNi Cantor alloy has excellent SLM processibility [11–13], *i.e.*, it has a large processing window to produce crack-free samples with low porosity levels. Nevertheless, with only small additions of TiAl (4 at. %), which are added to increase the strength, the SLM processibility of this alloy becomes significantly degraded. In the current investigation, solidification cracks associated with the presence of dendrites were seen to form in the $(CrMnFeCoNi)_{96}(TiAl)_4$ samples regardless of the AM processing conditions applied (Fig. 2a–c). According to previous studies, such solidification cracking is considered to occur in the partly solid state with the semi-solid zone being critical for the solidification cracking susceptibility [19]. A limited solidification range provides a narrow semi-solid mush and helps to reduce cracking. To better understand the influence of TiAl and Cr_3C_2 on the solidification behavior of CrMnFeCoNi, Thermo-Calc with the TCHEA3 database was used to simulate the Scheil solidification process of the different high-entropy alloys under study. The results are shown in Figs. 18 and 19 and Table 4. Apparently, the CrMnFeCoNi alloy has the narrowest solidification range ($\Delta T_{SL} = 168$ °C), which is beneficial for avoiding the development of cracks during solidification upon SLM. The addition of 4 at.% TiAl to the CrMnFeCoNi alloy leads to an immediate two-fold increase in ΔT_{SL} as compared to the pure alloy. Further additions of 2.5 at.% Cr_3C_2 reduces the ΔT_{SL} back to 274 °C. It is evident that both the CrMnFeCoNi and $(CrMnFeCoNi)_{96}(TiAl)_4 + Cr_3C_2$ alloys show relatively smaller solidification ranges, which we deem to be the primary reason why they are not prone to hot cracking. In contrast, the much larger solidification range for the $(CrMnFeCoNi)_{96}(TiAl)_4$ alloy leads to a larger semi-solid zone that increases the propensity for hot tearing; we consider this to be the origin of the solidification cracking in this alloy during SLM.

The variation in the solidification range of these high-entropy alloys can be ascribed to the additions of TiAl and C. Previous studies on nickel-base superalloys have indicated that Ti can cause a considerable reduction in solidus temperature, which expands the solidification range; C, on the other hand, slightly increases the solidus temperature and helps reduce the solidification range [25,26]. Given that the present alloys develop the same matrix (*i.e.*,

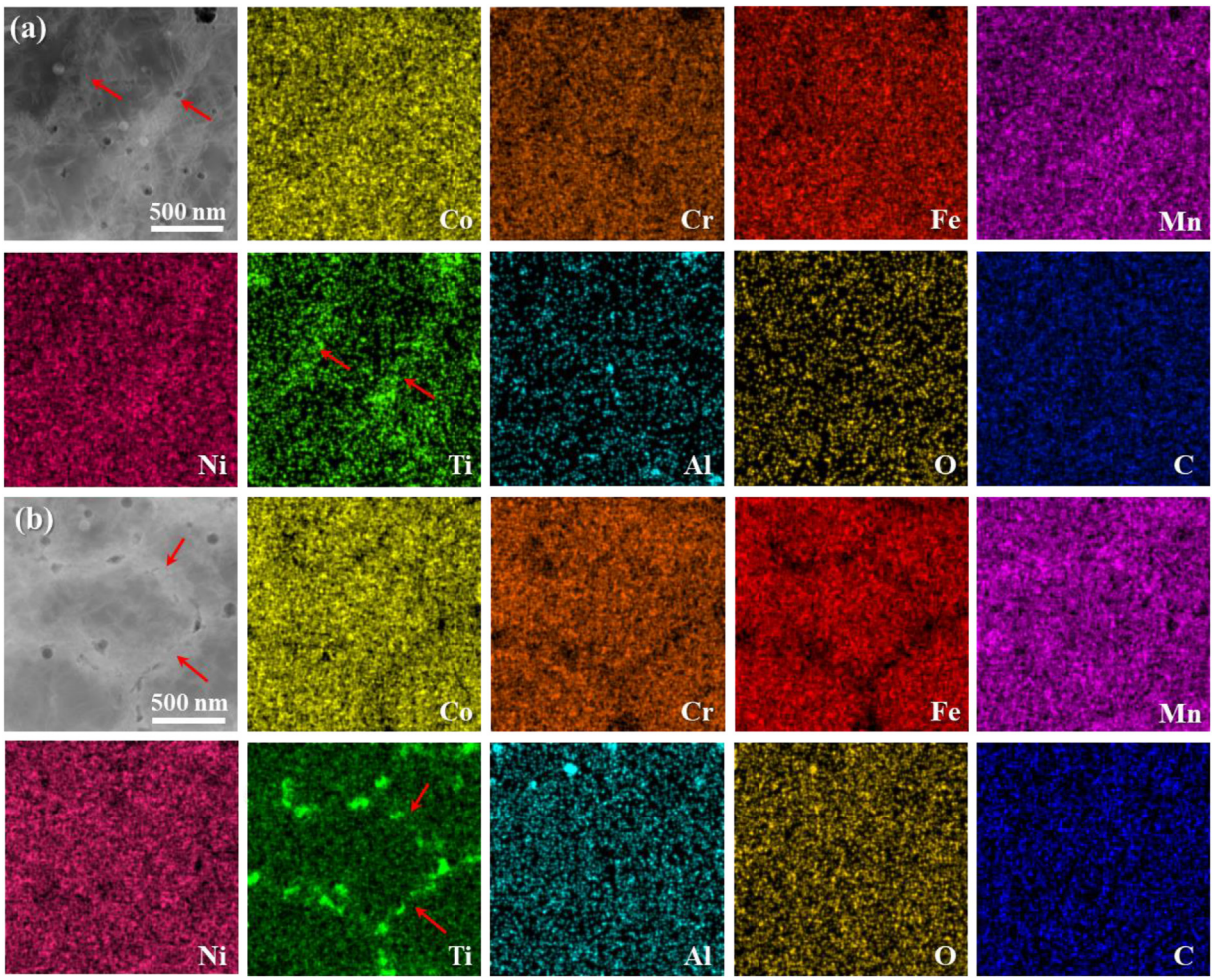

Fig. 11. TEM micrographs and EDS mapping analysis results of some cells in the as-printed (a) $(CrMnFeCoNi)_{96}(TiAl)_4$ and (b) $(CrMnFeCoNi)_{96}(TiAl)_4 + Cr_3C_2$ samples. The arrows indicate the cell boundaries.

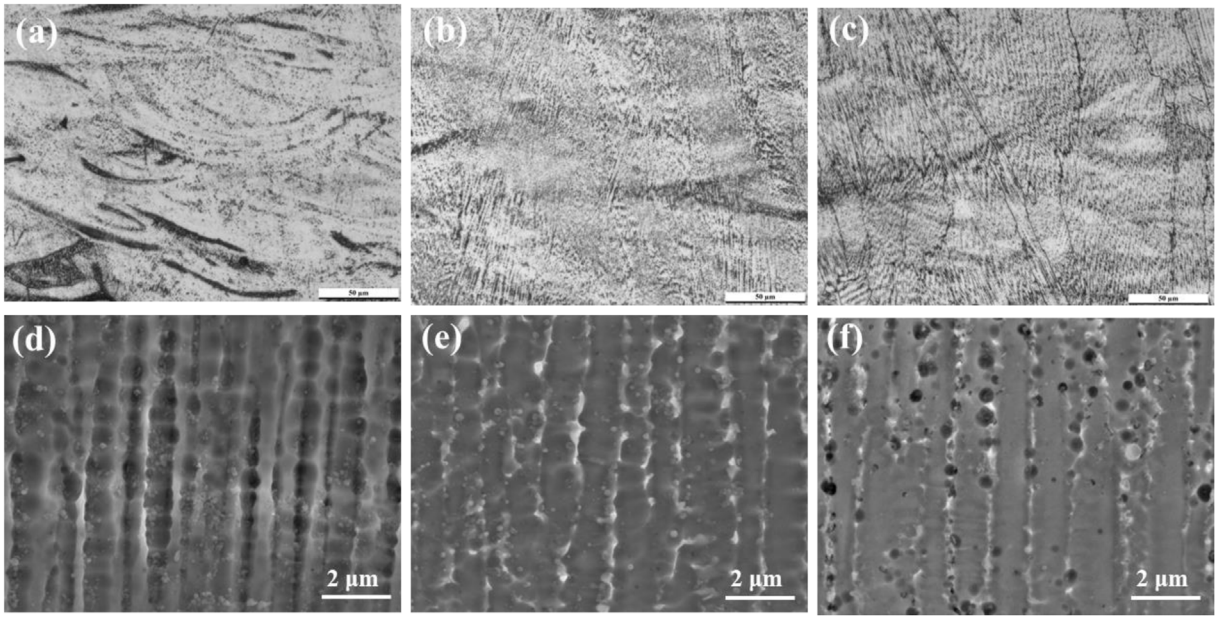

Fig. 12. Optical and scanning electron micrographs showing the cell structures in the as-printed $(CrMnFeCoNi)_{96}(TiAl)_4 + Cr_3C_2$ samples processed at (a, d) 250 W-120 μs, (b, e) 400 W-120 μs and in the (c, f) SLM-processed (400 W-120 μs) + aged sample.

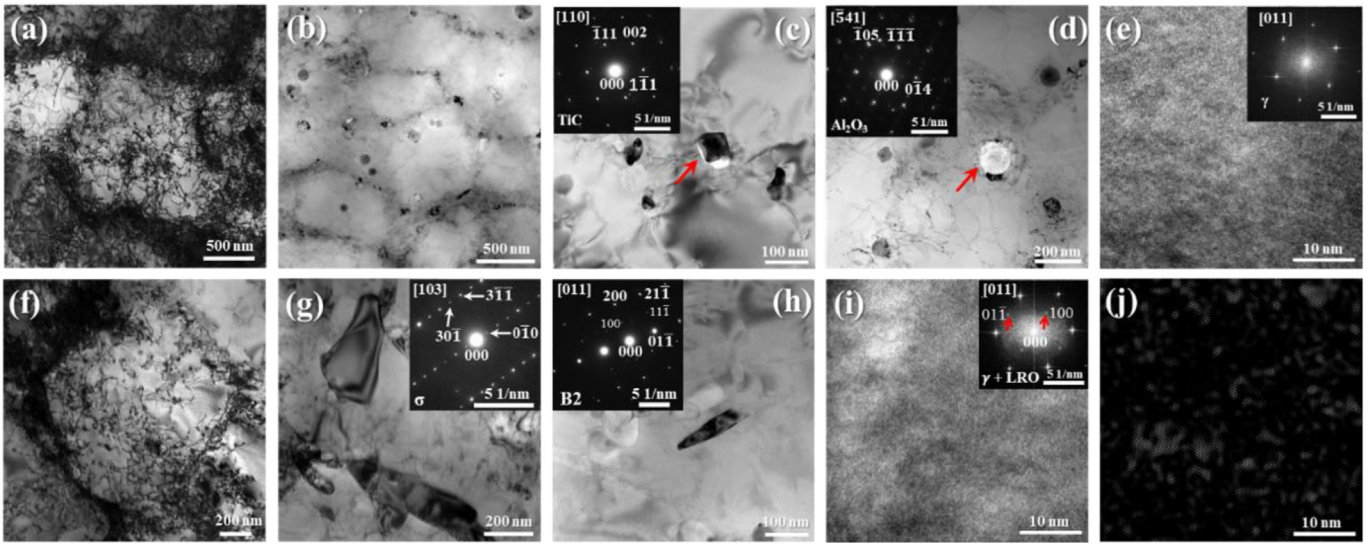

Fig. 13. TEM micrographs showing cell structures and precipitates in (a–e) an as-printed $(CrMnFeCoNi)_{96}(TiAl)_4 + Cr_3C_2$ sample and (f–j) a SLM-processed and aged $(CrMnFeCoNi)_{96}(TiAl)_4 + Cr_3C_2$ sample. The insets in (c),(d),(g) and (h) showing the selected area diffraction patterns (SADPs) of TiC, Al_2O_3, σ and B2 precipitates, respectively. (e) and (i) are high-resolution TEM images and their insets are FFT patterns from the matrix. (j) Inverse FFT image obtained using the superlattice reflections shown in (i) confirming the presence of long-range ordered $L1_2$ domains.

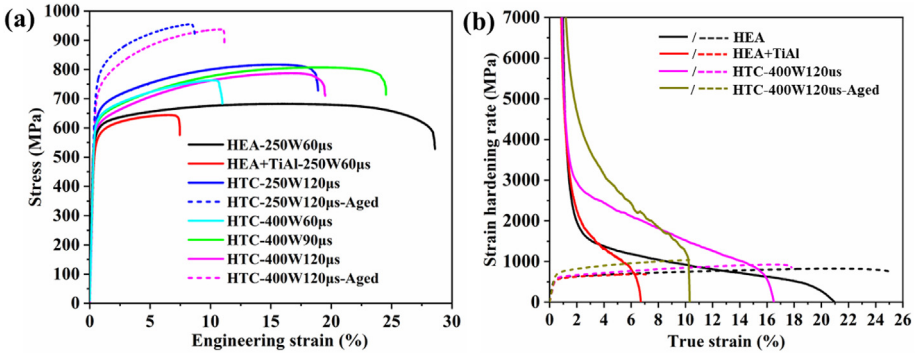

Fig. 14. (a) Engineering uniaxial tensile stress-strain curves, (b) true stress-strain curves and strain hardening rate-true strain curves of the as-printed CrMnFeCoNi, $(CrMnFeCoNi)_{96}(TiAl)_4$, $(CrMnFeCoNi)_{96}(TiAl)_4 + Cr_3C_2$ and SLM-processed + aged $(CrMnFeCoNi)_{96}(TiAl)_4 + Cr_3C_2$ samples. The HEA in the graphs refers to CrMnFeCoNi alloy while the HTC refers to $(CrMnFeCoNi)_{96}(TiAl)_4 + Cr_3C_2$ alloy.

Table 3
Tensile properties of the several SLM-processed HEAs investigated in this study.

Samples	Processing condition	YS (MPa)	UTS (MPa)	El (%)
CrMnFeCoNi	250 W-60 μs	569.7	682.5	28.3
$(CrMnFeCoNi)_{96}(TiAl)_4$	250 W-60 μs	550.0	644.3	7.1
$(CrMnFeCoNi)_{96}(TiAl)_4 + Cr_3C_2$	250 W-120 μs	633.1	807.2	18.5
$(CrMnFeCoNi)_{96}(TiAl)_4 + Cr_3C_2$	400 W-60 μs	616.2	763.4	10.6
$(CrMnFeCoNi)_{96}(TiAl)_4 + Cr_3C_2$	400 W-90 μs	615.7	736.3	24.1
$(CrMnFeCoNi)_{96}(TiAl)_4 + Cr_3C_2$	400 W-120 μs	594.5	787.4	19.1
$(CrMnFeCoNi)_{96}(TiAl)_4 + Cr_3C_2$	250 W-120 μs + Aged	752.9	955.6	8.2
$(CrMnFeCoNi)_{96}(TiAl)_4 + Cr_3C_2$	400 W-120 μs + Aged	710.6	937.7	11.2

an FCC γ matrix) as nickel-base superalloys during SLM, Ti and C are likely to play similar roles in affecting the solidification behavior. Moreover, the present TEM-EDS mapping analysis demonstrates that Ti tended to segregate to the cell and grain boundaries in the as-printed $(CrMnFeCoNi)_{96}(TiAl)_4$ alloy, which could be due to Ti being highly unfavorable for the stability of the γ matrix and is thus rejected to interdendritic regions during solidification. The segregation of Ti in the interdendritic regions indicates that the liquid during latter stages of solidification would be enriched in Ti. This means that the liquid during final solidification would have an even larger solidification range (>318 °C) and thus be more susceptible to solidification cracking in the case of $(CrMnFeCoNi)_{96}(TiAl)_4$ during SLM. In this sense, Ti segregation is undoubtedly the reason for the significant degradation in SLM processibility of the CrMnFeCoNi alloy. To counter this problem, the addition of Cr_3C_2 converts the continuous and segregated Ti at cell and grain boundaries into discrete TiC particles (Fig. 11), which helps to elevate the solidus temperature and thus reduces the solidification

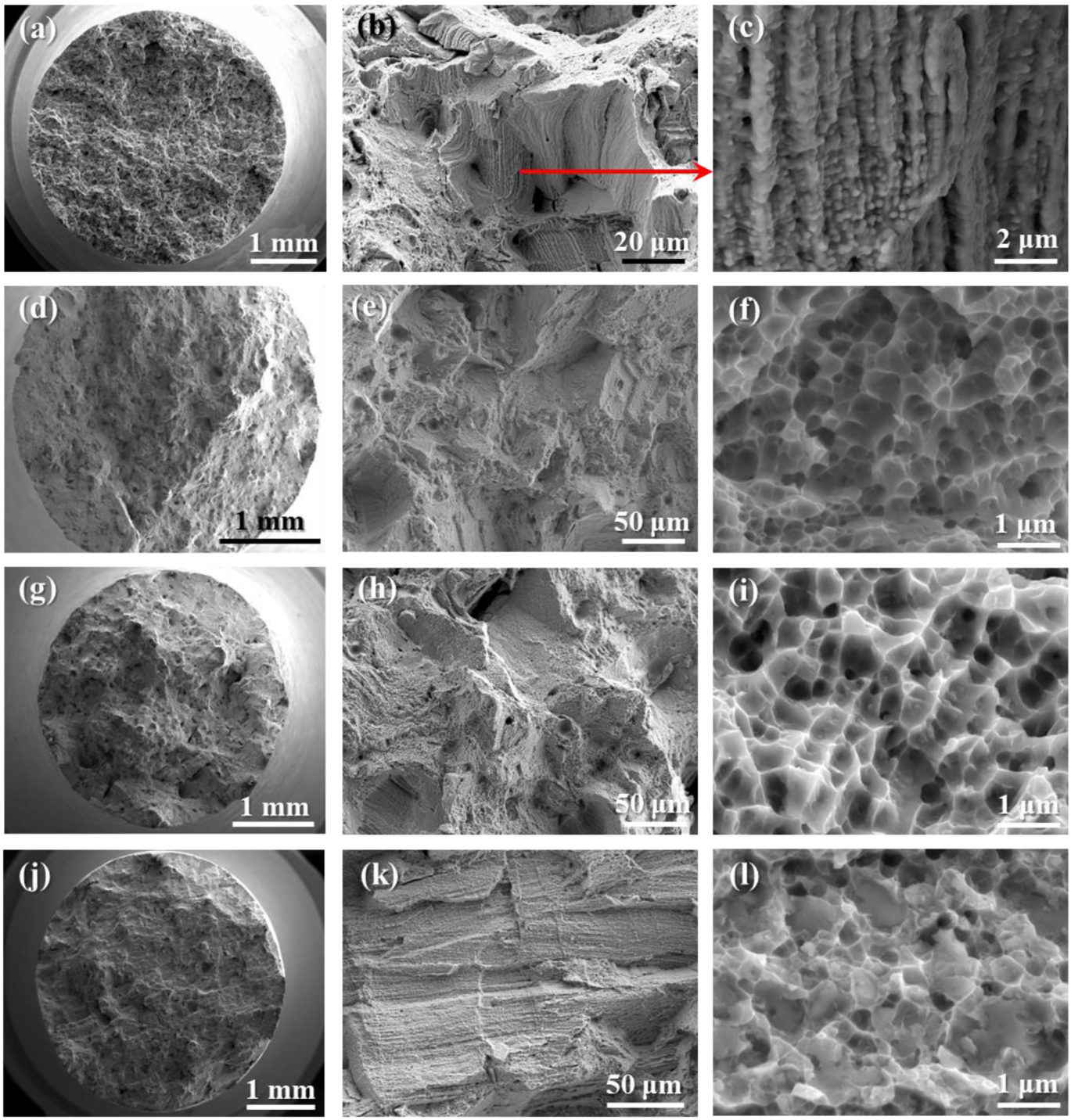

Fig. 15. SEM micrographs showing the fracture surfaces of the as-printed (a–c) $(CrMnFeCoNi)_{96}(TiAl)_4$, (d–f) $(CrMnFeCoNi)_{96}(TiAl)_4 + Cr_3C_2$ sample made with 250 W-120 μs, (g–i) $(CrMnFeCoNi)_{96}(TiAl)_4 + Cr_3C_2$ sample made with 400 W-120 μs and (j–l) SLM-processed (400 W-120 μs) + aged $(CrMnFeCoNi)_{96}(TiAl)_4 + Cr_3C_2$ sample.

range. We believe that this is the main reason for the successful suppression of solidification cracking during SLM of the $(CrMnFeCoNi)_{96}(TiAl)_4 + Cr_3C_2$ alloy (Fig. 2d–f).

The partition coefficient of C ($k_C = \frac{X_S}{X_L}$, where X_S and X_L are the mole fractions of C in the solid and liquid) was reported to be ~0.2 under equilibrium conditions in Ni-base superalloys [34]. Thus, C should be mainly concentrated along the cell and grain boundaries during solidification. Although EDS mapping results did not show obvious segregation of C at these boundaries (EDS is known, however, to be inaccurate in analysing light elements such as C), the formation of TiC particles along the cell and boundaries strongly suggests that C should have accumulated at these interdendritic regions.

While the susceptibility to solidification cracking of the high-entropy Cantor alloys investigated in this study can be rationalized in terms of their freezing ranges, this analysis has its limitations since it fails to account for the very last stages of the solidification path which are known to be important and can be

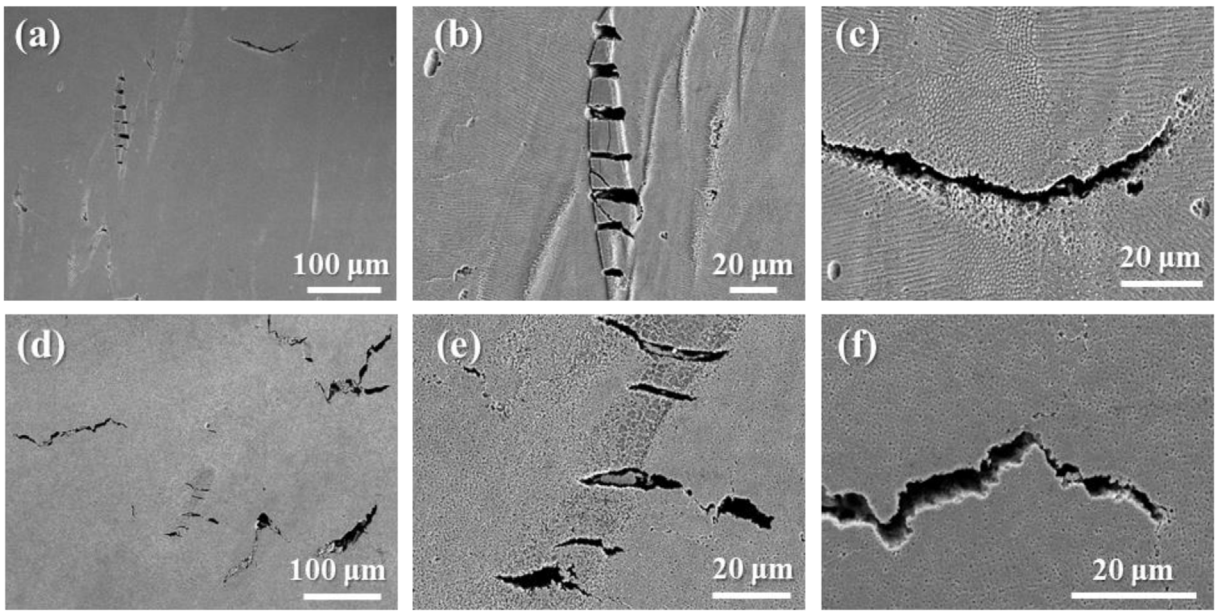

Fig. 16. SEM micrographs showing the longitudinal sections of (a–c) as-printed $(CrMnFeCoNi)_{96}(TiAl)_4$ and (d–f) SLM-processed and aged $(CrMnFeCoNi)_{96}(TiAl)_4 + Cr_3C_2$ samples after tensile testing.

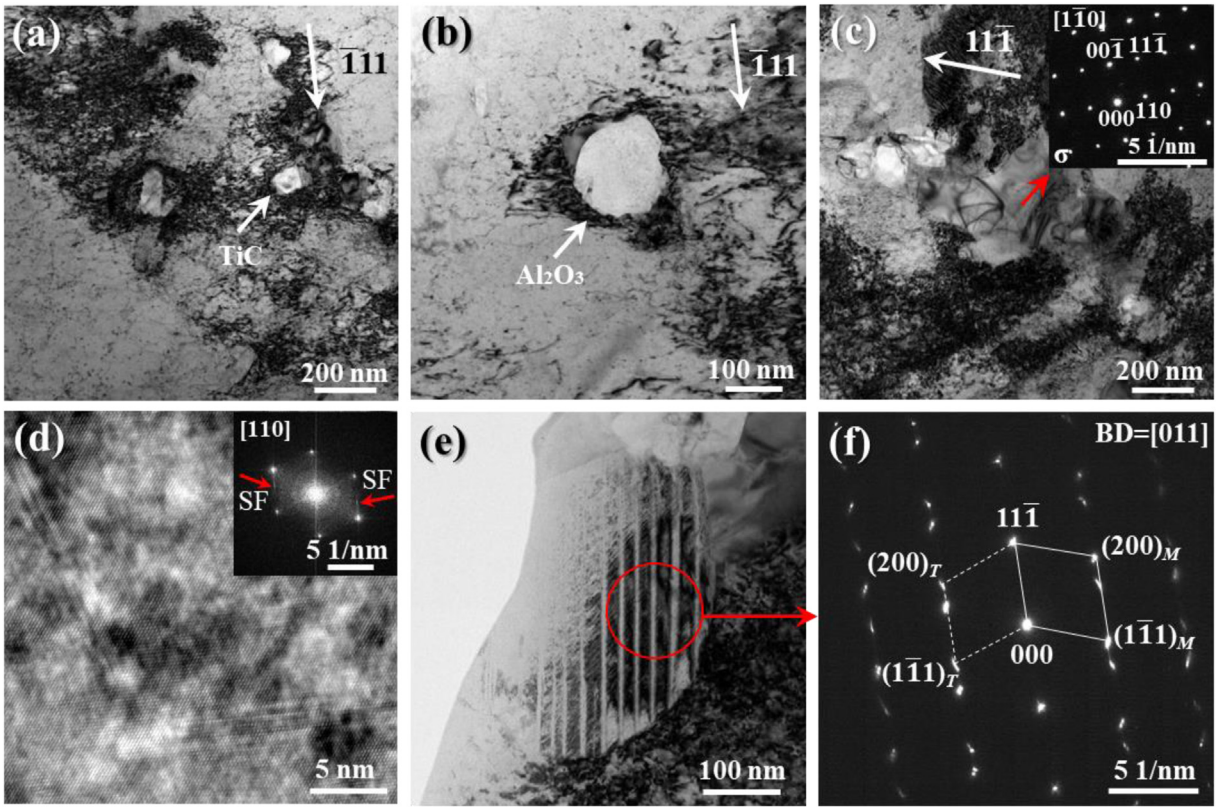

Fig. 17. (a–c) TEM micrographs showing the interaction between dislocations and precipitates in a SLM-processed and aged $(CrMnFeCoNi)_{96}(TiAl)_4 + Cr_3C_2$ sample after uniaxial tensile testing; (d) high-resolution TEM image and FFT pattern from the matrix (the inset) showing the presence of stacking faults (SFs) in the deformed sample; (e) TEM micrograph and (f) selected area diffraction pattern (SADP) showing the presence of twins in the deformed sample. The inset in (c) shows the SADP from a $\boldsymbol{\sigma}$ precipitate.

potentially decisive [35,36]. To examine the resistance to hot tearing in the regime, the solidification gradient is utilized. The solidification gradient, which takes account of the interplay between the strain rate of the solidifying solid (which promotes cracking) and the feeding rate of the liquid (which inhibits cracking) is an ideal solidification cracking index (SCI) for the late stage of solidification [27,37,38]. SCI plots of the solid fraction f_s versus $|dT/d(f_s^{1/2})|$ are displayed in Fig. 19 over the range $0 < f_s < 1.0$

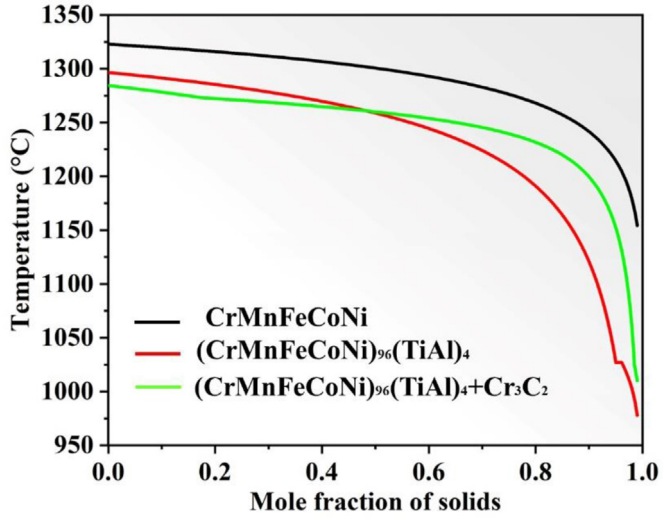

Fig. 18. Thermo-Calc computed solidification paths of CrMnFeCoNi, $(CrMnFeCoNi)_{96}(TiAl)_4$ and $(CrMnFeCoNi)_{96}(TiAl)_4 + Cr_3C_2$ samples under the Scheil condition.

Table 4
Solidification cracking index (SCI) values in the range of $0.87 < f_S < 0.94$ and Scheil freezing ranges of the three high-entropy alloys calculated based upon the Scheil solidification curves obtained using Thermo-Calc with TCHEA3 database.

HEA alloys	SCI (K)	Scheil freezing range (K)
CrMnFeCoNi	911.2	168
$(CrMnFeCoNi)_{96}(TiAl)_4$	3063.8	318
$(CrMnFeCoNi)_{96}(TiAl)_4$+$Cr_2C_3$	1547.7	274

and $0.87 < f_s < 0.94$. The SCI in the range $0.87 < f_s < 0.94$ (corresponding to $0.933 < f_s^{1/2} < 0.970$) is believed to reflect the cracking susceptibility of an alloy during the late stage of solidification [27]. One can see that the cracking index for $(CrMnFeCoNi)_{96}(TiAl)_4$ is predominantly higher than for the other two alloys over a wide solidification range ($0.2 < f_s < 0.94$). The alloy also shows the largest average SCI (= 3063.8) in the range of $0.87 < f_s < 0.94$ among all three HEAs (Table 4). A higher SCI in the late stage of solidification discourages the liquid feeding in the grain boundary regions and delays the bridging of separated grains due to thermal contraction, which increases the chance for cracking under stress/strain accumulation. In comparison, the average cracking indices in the range of $0.87 < f_s < 0.94$ for both CrMnFeCoNi and $(CrMnFeCoNi)_{96}(TiAl)_4 + Cr_3C_2$ are much smaller. This accounts for the poor SLM processibility of the $(CrMnFeCoNi)_{96}(TiAl)_4$ alloy and the excellent SLM processibility of the other two alloys. In general, the larger solidification range and higher cracking index in the later stage of solidification reinforce the severe susceptibility to hot cracking of the $(CrMnFeCoNi)_{96}(TiAl)_4$ alloy during SLM.

4.2. Microstructure-property relationship

The current experimental results demonstrate that with the presence of cracks in the as-printed $(CrMnFeCoNi)_{96}(TiAl)_4$ alloy samples, the alloy exhibits significantly reduced ductility due to its premature failure (Fig. 15a–c). In contrast, the $(CrMnFeCoNi)_{96}(TiAl)_4 + Cr_3C_2$ alloy samples show successfully suppressed hot cracking during SLM and as such exhibited an improvement in yield strength by ~50 MPa and a very significant improvement in ultimate tensile strength by ~100 MPa, as compared with as-printed CrMnFeCoNi. As both these as-printed alloys contain fine cell structures with high dislocation densities (Fig. 13) [11–13], the improvement in strength can be primarily attributed to the TiC and Al_2O_3 nano-precipitates (Fig. 13b–d) and solution strengthening from the dissolution of any Ti, Al and C solute atoms in the matrix. Aging led to substantial enhancement in both the yield and tensile strengths in the as-printed $(CrMnFeCoNi)_{96}(TiAl)_4 + Cr_3C_2$ alloy, which we mainly attribute to the formation of B2 and σ precipitates and the consequent precipitation hardening. Additionally, the aging-induced creation of LRO $L1_2$ domains in the γ matrix further contributed to the improved strengths of this alloy as the anti-phase boundary energy inherent in these ordered domains constitutes another strong barrier to dislocation motion.

To better understand the relative potency of the two strengthening mechanisms associated with aging, we consider analytical models for their effect. The improvement in strength induced by the LRO $L1_2$ domains, $\sigma_{ordering}$, can be estimated using the following relationship [39]:

$$\sigma_{ordering} = M\frac{\gamma_{APB}}{2b}\left(\sqrt{\frac{\gamma_{APB}d_s}{2T_L}}\ \frac{d_s}{L_s} - \frac{\pi}{4}\left(\frac{d_s}{L}\right)^2\right) \quad (2)$$

where M is the Taylor factor for FCC materials and equal to 3.06 [40], γ_{APB} is the anti-phase boundary energy, b is the Burgers vector (which is ~0.255 nm for the γ phase in CrMnFeCoNi [41]), d_s is the mean diameter of the LRO $L1_2$ domains, L_s is the spacing between the domains, T_L is the line tension of the dislocations and L is the center-to-center spacing between the LRO domains that can be

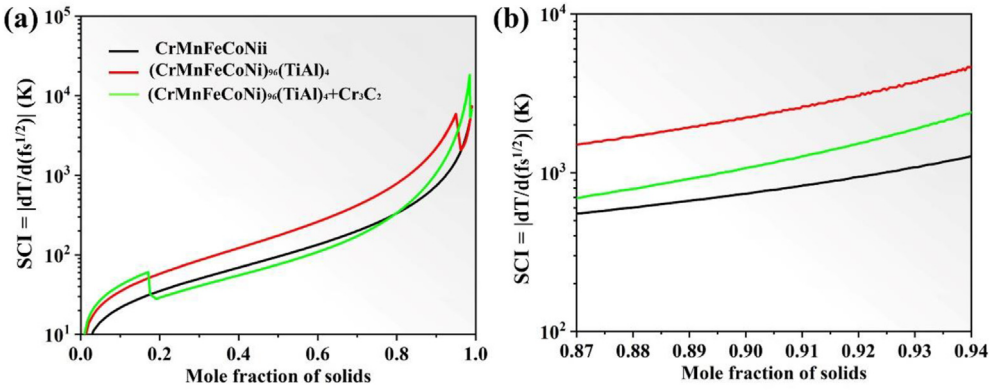

Fig. 19. Solidification cracking index (SCI) of the high-entropy alloys investigated in the present study based upon solidification curves calculated using Thermo-Calc with the TCHEA3 database. (a) SCI values over the full range of solid fractions, (b) SCI values of the last stage solidification in the range of 0.87–0.94.

evaluated from Ref. [42]:

$$L = \sqrt{\frac{8}{3\pi f}} d_s \tag{3}$$

where f is the volume fraction of the LRO domains. In eq. (2), L_s can be described by Ref. [39]:

$$L_s = \sqrt{\frac{8}{3\pi f}} d_s - d_s \tag{4}$$

and the dislocation line tension T_L from Ref. [43]:

$$T_L = \frac{Gb^2}{2} \tag{5}$$

The γ_{APB} of the LRO $L1_2$ domains has been estimated to be ~122 mJ/m^2 [44], d_s was measured to be ~2.27 nm and f is ~0.39. Thus, the contribution to the yield strength from the presence of the LRO $L1_2$ domains ($\sigma_{ordering}$) can be estimated to be on the order of 88 MPa.

The corresponding contribution to the strength from precipitation hardening, σ_{PPT}, is primarily induced by the mechanism of Orowan bypassing, where [45]:

$$\sigma_{PPT} = M \frac{0.4Gb}{\pi\lambda} \frac{\ln(2\bar{r}/b)}{\sqrt{1-\nu}} \tag{6}$$

$$\lambda = 2\bar{r}\left(\sqrt{\frac{\pi}{4f}} - 1\right) \tag{7}$$

$$\bar{r} = r\sqrt{2/3} \tag{8}$$

where $\nu = 0.31$ is Poisson's ratio for the γ matrix, λ is the edge-to-edge inter-particle spacing, $\bar{r}$ is the mean radius of circular cross sections in different random planes for a spherical precipitate, $r = 90.2$ nm is the measured mean precipitate radius, and f ~1.4% is the volume fraction of the precipitates. Using these values, the contribution to the strength from Orowan bypassing, σ_{PPT} can be estimated to be ~64 MPa. Based on the calculations, the total contribution to the strength of the (CrMnFeCoNi)96(TiAl)4 + Cr_3C_2 alloy from LRO $L1_2$ domains and from B2 and σ precipitates is ~152 MPa, which is comparable to the increment in the yield strength from the SLM + HIPed structure to the aged structure (~140 MPa). Accordingly, we can conclude that the strength improvement induced by aging is principally associated with the B2 and σ precipitation and the formation of LRO $L1_2$ domains.

5. Conclusions

- The well-known CrMnFeCoNi Cantor high-entropy alloy, when strengthened with TiAl particles ((CrMnFeCoNi)$_{96}$(TiAl)$_4$) for additive manufacturing using selective laser melting (SLM), can experience severe solidification cracking. This was found to be associated with the segregation of Ti to cell and grain boundaries which served to widen the solidification range and increase the alloy's susceptibility to hot cracking.
- The addition of 2.5 at.% Cr_3C_2 into the (CrMnFeCoNi)$_{96}$(TiAl)$_4$ alloy during SLM transformed Ti segregated at cell and grain boundaries into discrete TiC particles, which greatly reduced the solidification range and the cracking index in the later stages of solidification. This acted to fully suppress hot tearing.
- The as-printed (CrMnFeCoNi)$_{96}$(TiAl)$_4$ + Cr_3C_2 samples were found to consist of cell structures and a small number of Al_2O_3 and TiC particles. Aging at 650 °C leads to the formation of a high density of long-range ordered (LRO) $L1_2$ domains and significant B2 and σ precipitation.
- The as-printed (CrMnFeCoNi)$_{96}$(TiAl)$_4$ displays a reduced yield strength and significantly reduced ductility due to the presence of cracks when compared with the SLM-processed CrMnFeCoNi alloy. With the addition of Cr_3C_2, the as-printed (CrMnFeCoNi)$_{96}$(TiAl)$_4$ + Cr_3C_2 samples showed an enhanced yield strength and a considerably improved ultimate tensile strength.
- Aging treatments significantly enhanced the yield and ultimate tensile strengths of the SLM-processed (CrMnFeCoNi)$_{96}$(TiAl)$_4$ + Cr_3C_2 alloy while maintaining good ductility. The LRO domains and precipitation of B2 and σ are deemed to be responsible for the improvement in alloy strength by effectively impeding dislocation motion during plastic deformation.

Credit author statement

Xintian Wang: Investigation, Visualization, Writing-original draft, Writing-review & editing. Zhiyong Ji: Investigation. Robert O. Ritchie: Writing - review & editing. Ilya Okulov: Writing - review & editing. Juergen Eckert: Writing - review & editing. Chunlei Qiu: Funding acquisition, Conceptualization, Resources, Project administration, Supervision, Visualization, Writing-original draft, Writing - review & editing.

Declaration of competing interest

The authors declare that they have no known competing financial interests or personal relationships that could have appeared to influence the work reported in this paper.

Data availability

Data will be made available on request.

Acknowledgments

Funding: This work was supported by the National Key Research and Development Program from the Ministry of Science and Technology of the People's Republic of China under Grant 2018YFB0703400.

Appendix A. Supplementary data

Supplementary data to this article can be found online at https://doi.org/10.1016/j.mtadv.2023.100371.

References

[1] Y. Zhang, T.T. Zuo, Z. Tang, M.C. Gao, K.A. Dahmen, P.K. Liaw, Z.P. Lu, Microstructures and properties of high-entropy alloys, Prog. Mater. Sci. 61 (2014) 1–93, https://doi.org/10.1016/j.pmatsci.2013.10.001.
[2] D.B. Miracle, O.N. Senkov, A critical review of high entropy alloys and related concepts, Acta Mater. 122 (2017) 448–511, https://doi.org/10.1016/j.actamat.2016.08.081.
[3] D. Raabe, R.O. Ritchie, E.P. George, High-entropy alloys, Nat. Rev. Mater. 4 (2019) 515–534, https://doi.org/10.1038/s41578-019-0121-4.
[4] L. Fan, T. Yang, Y. Zhao, J. Luan, G. Zhou, H. Wang, Z. Jiao, C.-T. Liu, Ultrahigh strength and ductility in newly developed materials with coherent nanolamellar architectures, Nat. Commun. 11 (2020) 6240, https://doi.org/10.1038/s41467-020-20109-z.
[5] B. Gludovatz, A. Hohenwarter, D. Catoor, E.H. Chang, E.P. George, R.O. Ritchie, A fracture-resistant high-entropy alloy for cryogenic applications, Science 345 (2014) 1153, https://doi.org/10.1126/science.1254581.

[6] J.Y. He, W.H. Liu, H. Wang, Y. Wu, X.J. Liu, T.G. Nieh, Z.P. Lu, Effects of Al addition on structural evolution and tensile properties of the FeCoNiCrMn high-entropy alloy system, Acta Mater. 62 (2014) 105–113, https://doi.org/10.1016/j.actamat.2013.09.037.
[7] N. Eißmann, U. Mühle, U. Gaitzsch, G. Walther, T. Weißgärber, B. Kieback, Precipitation hardening of high entropy alloy CoCrFeMnNi containing titanium, J. Alloys Compd. 857 (2021), 157610, https://doi.org/10.1016/j.jallcom.2020.157610.
[8] J. Kang, N. Park, J.-K. Kim, J.H. Park, Role of recrystallization and second phases on mechanical properties of $(CoCrFeMnNi)_{95.2}Al_{3.2}Ti_{1.6}$ high entropy alloy, Mater. Sci. Eng. A 814 (2021), 141249, https://doi.org/10.1016/j.msea.2021.141249.
[9] J.Y. He, H. Wang, H.L. Huang, X.D. Xu, M.W. Chen, Y. Wu, X.J. Liu, T.G. Nieh, K. An, Z.P. Lu, A precipitation-hardened high-entropy alloy with outstanding tensile properties, Acta Mater. 102 (2016) 187–196, https://doi.org/10.1016/j.actamat.2015.08.076.
[10] Y.Y. Zhao, H.W. Chen, Z.P. Lu, T.G. Nieh, Thermal stability and coarsening of coherent particles in a precipitation-hardened $(NiCoFeCr)_{94}Ti_2Al_4$ high-entropy alloy, Acta Mater. 147 (2018) 184–194, https://doi.org/10.1016/j.actamat.2018.01.049.
[11] Z.G. Zhu, Q.B. Nguyen, F.L. Ng, X.H. An, X.Z. Liao, P.K. Liaw, S.M.L. Nai, J. Wei, Hierarchical microstructure and strengthening mechanisms of a CoCrFeNiMn high entropy alloy additively manufactured by selective laser melting, Scripta Mater. 154 (2018) 20–24, https://doi.org/10.1016/j.scriptamat.2018.05.015.
[12] R. Li, P. Niu, T. Yuan, P. Cao, C. Chen, K. Zhou, Selective laser melting of an equiatomic CoCrFeMnNi high-entropy alloy: processability, non-equilibrium microstructure and mechanical property, J. Alloys Compd. 746 (2018) 125–134, https://doi.org/10.1016/j.jallcom.2018.02.298.
[13] B. Dovgyy, A. Piglione, P.A. Hooper, M.-S. Pham, Comprehensive assessment of the printability of CoNiCrFeMn in laser powder bed fusion, Mater. Des. 194 (2020), 108845, https://doi.org/10.1016/j.matdes.2020.108845.
[14] Z. Sun, X.P. Tan, M. Descoins, D. Mangelinck, S.B. Tor, C.S. Lim, Revealing hot tearing mechanism for an additively manufactured high-entropy alloy via selective laser melting, Scripta Mater. 168 (2019) 129–133, https://doi.org/10.1016/j.scriptamat.2019.04.036.
[15] Z. Sun, X. Tan, C. Wang, M. Descoins, D. Mangelinck, S.B. Tor, E.A. Jägle, S. Zaefferer, D. Raabe, Reducing hot tearing by grain boundary segregation engineering in additive manufacturing: example of an $Al_xCoCrFeNi$ high-entropy alloy, Acta Mater. 204 (2021), 116505, https://doi.org/10.1016/j.actamat.2020.116505.
[16] Y. Su, S. Luo, Z. Wang, Microstructure evolution and cracking behaviors of additively manufactured $Al_xCrCuFeNi_2$ high entropy alloys via selective laser melting, J. Alloys Compd. 842 (2020), 155823, https://doi.org/10.1016/j.jallcom.2020.155823.
[17] S. Luo, C. Zhao, Y. Su, Q. Liu, Z. Wang, Selective laser melting of dual phase $AlCrCuFeNi_x$ high entropy alloys: formability, heterogeneous microstructures and deformation mechanisms, Addit. Manuf. 31 (2020), 100925, https://doi.org/10.1016/j.addma.2019.100925.
[18] X.T. Wang, X.Y. Pan, P.Y. Sun, C.L. Qiu, Significant enhancement in tensile strength and work hardening rate in CoCrFeMnNi by adding TiAl particles via selective laser melting, Mater. Sci. Eng. A 831 (2022), 142285, https://doi.org/10.1016/j.msea.2021.142285.
[19] J. Zhang, R.F. Singer, Hot tearing of nickel-based superalloys during directional solidification, Acta Mater. 50 (2002) 1869–1879, https://doi.org/10.1016/S1359-6454(02)00042-3.
[20] D.G. Eskin, L. Katgerman, A quest for a new hot tearing criterion, Metall. Mater. Trans. A 38 (2007) 1511–1519, https://doi.org/10.1007/s11661-007-9169-7.
[21] E. Chauvet, P. Kontis, E.A. Jägle, B. Gault, D. Raabe, C. Tassin, J.-J. Blandin, R. Dendievel, B. Vayre, S. Abed, G. Martin, Hot cracking mechanism affecting a non-weldable Ni-based superalloy produced by selective electron Beam Melting, Acta Mater. 142 (2018) 82–94, https://doi.org/10.1016/j.actamat.2017.09.047.
[22] I. Farup, J.M. Drezet, M. Rappaz, In situ observation of hot tearing formation in succinonitrile-acetone, Acta Mater. 49 (2001) 1261–1269, https://doi.org/10.1016/S1359-6454(01)00013-1.
[23] J.H. Martin, B.D. Yahata, J.M. Hundley, J.A. Mayer, T.A. Schaedler, T.M. Pollock, 3D printing of high-strength aluminium alloys, Nature 549 (2017) 365–369, https://doi.org/10.1038/nature23894.
[24] Y.T. Tang, C. Panwisawas, J.N. Ghoussoub, Y. Gong, J.W.G. Clark, A.A.N. Németh, D.G. McCartney, R.C. Reed, Alloys-by-design: application to new superalloys for additive manufacturing, Acta Mater. 202 (2021) 417–436, https://doi.org/10.1016/j.actamat.2020.09.023.
[25] Z. Sun, Y. Ma, D. Ponge, S. Zaefferer, E.A. Jägle, B. Gault, A.D. Rollett, D. Raabe, Thermodynamics-guided alloy and process design for additive manufacturing, Nat. Commun. 13 (2022) 4361, https://doi.org/10.1038/s41467-022-31969-y.
[26] W. Zhou, Y. Tian, Q. Tan, S. Qiao, H. Luo, G. Zhu, D. Shu, B. Sun, Effect of carbon content on the microstructure, tensile properties and cracking susceptibility of IN738 superalloy processed by laser powder bed fusion, Addit. Manuf. 58 (2022), 103016, https://doi.org/10.1016/j.addma.2022.103016.
[27] S. Kou, A criterion for cracking during solidification, Acta Mater. 88 (2015) 366–374, https://doi.org/10.1016/j.actamat.2015.01.034.
[28] P.A. Hooper, Melt pool temperature and cooling rates in laser powder bed fusion, Addit. Manuf. 22 (2018) 548–559, https://doi.org/10.1016/j.addma.2018.05.032.
[29] A. De, C.A. Walsh, S.K. Maiti, H.K.D.H. Bhadeshia, Prediction of cooling rate and microstructure in laser spot welds, Sci. Technol. Weld. Join. 8 (2003) 391–399, https://doi.org/10.1179/136217103225005633.
[30] X.Y. Pan, C.L. Qiu, Promoting columnar-to-equiaxed transition in AlCoCrFeNi high entropy alloy during selective laser melting by adding Cr_3C_2, Mater. Res. Lett. 10 (2022) 788–796, https://doi.org/10.1080/21663831.2022.2106798.
[31] X.T. Wang, C.L. Qiu, Effect of aging temperature on microstructure and mechanical properties of laser melted and hot isostatically pressed $(CoCrFeMnNi)_{96}(TiAl)_4$ alloy, J. Alloys Compd. 936 (2023), 168317, https://doi.org/10.1016/j.jallcom.2022.168317.
[32] P.Y. Sun, C.L. Qiu, Influence of addition of TiAl particles on microstructural and mechanical property development in a selectively laser melted stainless steel, Mater. Sci. Eng. A 826 (2021), 141925, https://doi.org/10.1016/j.msea.2021.141925.
[33] C.L. Qiu, Y.J. Liu, H.H. Liu, Influence of addition of TiAl particles on microstructural and mechanical property development in Invar 36 processed by laser powder bed fusion, Addit. Manuf. 48 (2021), 102457, https://doi.org/10.1016/j.addma.2021.102457.
[34] J.C. Lippold, S.D. Kiser, J.N. DuPont, Welding Metallurgy and Weldability of Nickel-Base Alloys, John Wiley & Sons2011.
[35] P. Kontis, E. Chauvet, Z. Peng, J. He, A.K. da Silva, D. Raabe, C. Tassin, J.-J. Blandin, S. Abed, R. Dendievel, B. Gault, G. Martin, Atomic-scale grain boundary engineering to overcome hot-cracking in additively-manufactured superalloys, Acta Mater. 177 (2019) 209–221, https://doi.org/10.1016/j.actamat.2019.07.041.
[36] A. Hariharan, L. Lu, J. Risse, A. Kostka, B. Gault, E.A. Jägle, D. Raabe, Misorientation-dependent solute enrichment at interfaces and its contribution to defect formation mechanisms during laser additive manufacturing of superalloys, Phys. Rev. Mater. 3 (2019), 123602, https://doi.org/10.1103/PhysRevMaterials.3.123602.
[37] M. Rappaz, J.M. Drezet, M. Gremaud, A new hot-tearing criterion, Metall. Mater. Trans. A 30 (1999) 449–455, https://doi.org/10.1007/s11661-999-0334-z.
[38] M. Rappaz, A. Jacot, W.J. Boettinger, Last-stage solidification of alloys: theoretical model of dendrite-arm and grain coalescence, Metall. Mater. Trans. A 34 (2003) 467–479, https://doi.org/10.1007/s11661-003-0083-3.
[39] R.W. Kozar, A. Suzuki, W.W. Milligan, J.J. Schirra, M.F. Savage, T.M. Pollock, Strengthening mechanisms in polycrystalline multimodal nickel-base superalloys, Metall. Mater. Trans. A 40 (2009) 1588–1603, https://doi.org/10.1007/s11661-009-9858-5.
[40] F. Otto, A. Dlouhy, C. Somsen, H. Bei, G. Eggeler, E.P. George, The influences of temperature and microstructure on the tensile properties of a CoCrFeMnNi high-entropy alloy, Acta Mater. 61 (2013) 5743–5755, https://doi.org/10.1016/j.actamat.2013.06.018.
[41] J.Y. He, C. Zhu, D.Q. Zhou, W.H. Liu, T.G. Nieh, Z.P. Lu, Steady state flow of the FeCoNiCrMn high entropy alloy at elevated temperatures, Intermetallics 55 (2014) 9–14, https://doi.org/10.1016/j.intermet.2014.06.015.
[42] A.J. Ardell, Precipitation hardening, Metall. Trans. A 16 (1985) 2131–2165, https://doi.org/10.1007/BF02670416.
[43] B. Reppich, Some new aspects concerning particle hardening mechanisms in γ' precipitating Ni-base alloys—I. Theoretical concept, Acta Metall. 30 (1982) 87–94, https://doi.org/10.1016/0001-6160(82)90048-7.
[44] J. Miao, C. Slone, S. Dasari, M. Ghazisaeidi, R. Banerjee, E.P. George, M.J. Mills, Ordering effects on deformation substructures and strain hardening behavior of a CrCoNi based medium entropy alloy, Acta Mater. 210 (2021), 116829, https://doi.org/10.1016/j.actamat.2021.116829.
[45] H. Wen, T.D. Topping, D. Isheim, D.N. Seidman, E.J. Lavernia, Strengthening mechanisms in a high-strength bulk nanostructured Cu–Zn–Al alloy processed via cryomilling and spark plasma sintering, Acta Mater. 61 (2013) 2769–2782, https://doi.org/10.1016/j.actamat.2012.09.036.